OPTIMIZATION OF COMPOSITE CARRIAGE FOR A COORDINATE MEASUREMENT MACHINE

by

Marco Lombardi

Thesis submitted to the Faculty of the

Virginia Polytechnic Institute and State University

in partial fulfillment of the requirements for the degree of

MASTER OF SCIENCE

in

Aerospace and Ocean Engineering

APPROVED:

R.T.Haftka, Chairmen

R.K. Kapania

Z. Gürdal

June, 1994

Blacksburg, Virginia

Optimization of Composite Carriage for a Coordinate Measurement Machine

by

Marco Lombardi

Committee Chairman: Dr. R.T. Haftka

Aerospace and Ocean Engineering

(ABSTRACT)

The growing need for high quality and reliability of products requires the control of the accuracy of dimensions and shape of product components. Coordinate Measurement Machines (CMM) are now able to measure the dimensions and/or the shape of objects with submicron precision. The desire for high-speed measurement, has stimulated the interest of CMM manufacturers in the use of composite materials for the structure of their machines. Composites are lighter than conventional materials, and are generally less affected by temperature changes.

In cooperation with one of the major European CMM manufacturers, the problem of redesigning a steel carriage of a CMM, from composite materials component is considered. A simple strength-of-materials based calculation is used to design a prototype of the carriage, which is built and mounted on the machine to be tested.

A NASTRAN finite element model of the composite component is created to analyze more accurately the behavior of the composite structure. Structural optimization is next performed to seek minimum weight and maximum stiffness designs of the structural component.

This Thesis is dedicated to

Melania
Roberto and MariaLuisa

Acknowledgments

Dr. Rafi T. Haftka - Being his student definitely a great experience. This alone deserve my best acknowledgments and thanks. I just don't have enough space here for all the rest.

Prof. Carlo Cinquini - for being such a patience advisor, and for his support during all these years.

Dr. Zafer Gürdal and Dr. R. K. Kapania - for serving in my committee and reading all my thesis.

Dr. Hayden O. Griffin - for teaching me the ABD of composite materials.

Dr. Ron Kriz - for opening my eyes to the world of scientific visualization.

Dr. Somanath "GE" Nagendra - because when you need help he can be the best, and when it comes to bother you he is so amazing (Go Home !).

Hugh Weiss - for all the times that he patiently fixed my computer problems.

Mike Wong - for his Nastran on-line support.

Barbara Grossman - manuals manuals manuals.

Paolo Barbieri - for being such a great friend, and good team-mate in the building of the carriage.

Mr. Giovanni Castiglioni and all the staff who worked on the carriage at Monfrini - for the great job they did.

Mr. Cerati - for introducing me to the fine art of getting the impossible things done and for the great experience at Speroni.

Jason, Pradeep, Satish, Tom, Ximing - for all the good time, the arguments, and the challenging records that we had in the office.

Warner Brothers and Bill Watterson - because there is nothing more relaxing than watching the Looney Tunes and read Calvin and Hobbes.

Mr. Beppe Speroni - afterall it was his carriage.

Table of Contents

List of Figures

List of Tables

1 Introduction

1.1 Coordinate Measuring Machines

In recent years, mass production factories has faced increasingly stringent requirements on the quality and the reliability of their products. Quality and reliability often depend on the geometric accuracy of components. To enforce the required accuracy we need to measure the dimensions of possibly every component, and compare them to the prescribed dimensions, and given tolerances.

Dimensions are measured by coordinate measuring machines (CMM, also called inspection machines or inspection robots). A CMM is a machine that scans the surface of an object in a discrete manner, measuring the coordinates of a number of given points of the surface of the object. The coordinates of all measured points are then compared to nominal values, or used to reconstruct the shape of the object. The complexity of the piece, and the required precision, determine the minimum number of points we need to identify the geometry of the piece.

Inspection machines based upon artificial vision are being developed and introduced to allow the acquisition of entire surfaces or pieces at once. However, almost all current systems are still based on touch sensors, i.e. sensors that physically touch the surface of the piece, allowing the acquisition of only one point at a time. The inspection speed, defined as the number of points measured in a unit of time, is therefore very important. By speeding up the inspection rate we reduce the amount of time required to measure a piece.

A great effort is being made by CMM manufacturers to improve machine performance. The weight of the machine is often a serious obstacle to increasing point acquisition speed. Large masses cannot be accelerated or decelerated fast enough, and also result in more slowly damped vibrations. Speroni, one of the leading European CMM manufacturers, has been working for more than two decades to improve the performance of their machines, recently exploring the possibility of using new materials for reducing their weights without sacrifying the stiffness.

In the present work, a possible solution to this problem is presented. A composite material prototype of the carriage for one of their machines is designed, built, and used to replace the old steel one. The prototype is then analyzed and optimized for minimum weight and minimum thermal deformation.

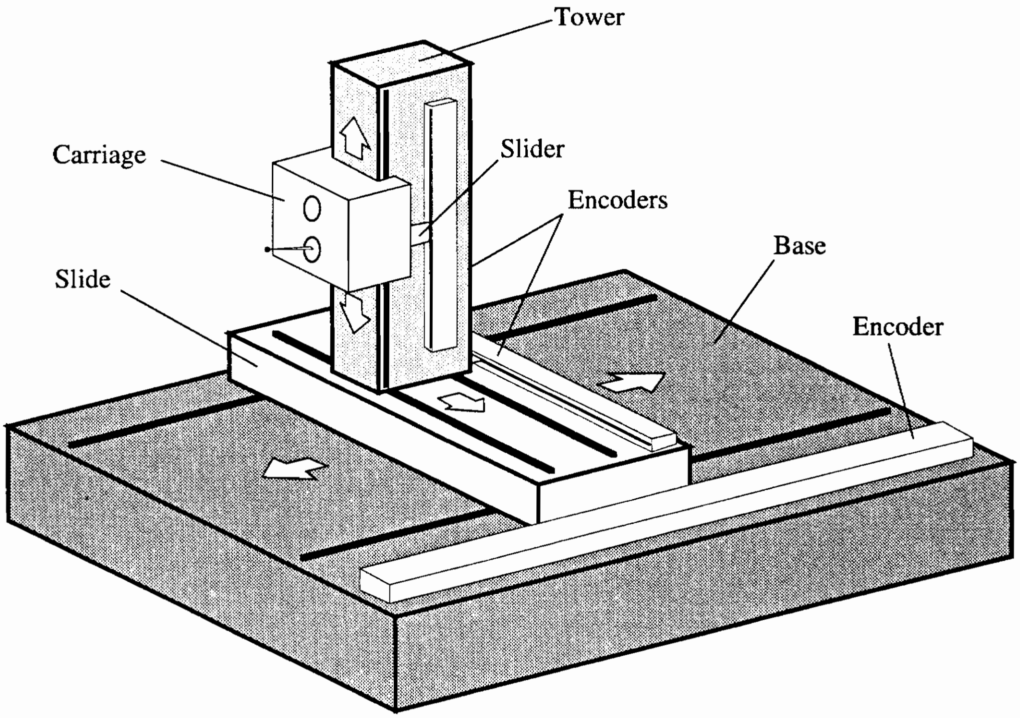

Figure 1.1 - Basic layout of the typical Speroni CMM.

1.2 History of the Project

Speroni's CMM line consists of three robots, of three different sizes, depending on the maximum size of the object that the robot can measure. The robots are completely made of steel and are the result of modifications of twenty-year-old initial structures. The principal requirement for the structure of a CMM is stiffness. Deformations of the structure caused by the self weight, and the dynamic loads induced by the sudden motion of the machine, affect the measurements in a way that, in most cases, is highly unpredictable. High stiffness structures reduce errors due to static and dynamic deformation. Thermal loads are also an important issue. The highest precision is in fact reached in controlled lab environments, but more often than not machines have to operate in shop-floor environments, where the temperature can typically change in a 40°C range.

Different strategies have been used by CMM manufacturers in order to reduce the effects of temperature on the precision and repeatability of the measurements. The designer of Speroni's robots wanted to give the structures large thermal inertia by increasing structural thicknesses, so that thermal deformations take longer to occur. The machine measures a sample of known position and dimensions at regular time intervals, resetting some internal parameters, such as the origin of the internal coordinate system. This allows it to compensate for thermal deformations. The thermal inertia of the structure reduces thermal effects on the structure between two consecutive resets. A side effect of this strategy is the increased weight of the structure.

On most of the pieces one needs to inspect, the measured points are very close one to another, and movements of the robots involve mostly acceleration and deceleration. Thus what determines the measurement speed is the maximum value of acceleration (positive and negative) rather than the velocity. The weight of the structure limits the acceleration, with high values causing problems in the mechanical transmission of the robot, and disrupting the regularity of its motion. Also, the oscillations caused by the large accelerations do not allow measuring coordinates until the oscillations are damped out.

A finite element analysis of the steel carriage of the largest Speroni's machine, carried out by Paolo Manzino [1], revealed that the structure was over designed with respect to strength and stiffness requirements. It was roughly estimated that an optimized structure could be twenty percent lighter than the present one. Despite the improved performance obtainable with a lighter structure, the cost of designing a new steel structure was considered too high, compared with the possible improvement.

In the past Speroni built a prototype of one of their robots, with the carriage and the tower made with carbon fiber composite tubes, that allowed quadrupling the value of the accelerations of the robot along two of the three machine main axes. However the carriage, designed for a particular application, could not replace the standard steel one mounted on other machines. Also with steel encoders and bearing guides used on the new composite tower, a new problem arose. The different thermal expansion coefficients caused bending of the tower, introducing an unpredictable source of error in the measurements.

Despite these problems the positive results, achieved without accurate analysis, demonstrated the great potential for improvement by the use of composites. The use of new materials was then considered for obtaining a structure that could be light, stiff, and little affected by temperature changes, and thus able to substantially improve the performance of the CMM.

This was the point at which I started my work under the guidance of Prof. Cinquini of the Department of Structural Mechanics of the University of Pavia, and Prof. Haftka of the Aerospace and Ocean Department at Virginia Tech. We decided that the carriage could represent a good starting point, being the smallest part of the structure but also one that is constantly moved. At that time an experienced engineer, Mr. Guzzinati, was in charge of the redesign of the carriage. The department at Pavia was asked to verify Mr. Guzzinati's new design, from a structural point of view, through finite element analysis and laboratory tests. I was to explore an alternate design by structural optimization at Virginia Tech. Among all available finite element analysis packages we decided to use MSC/NASTRAN for the modeling. NASTRAN had a module for structural optimization and sensitivity analysis, and it was available both at Virginia Tech and at the University of Pavia.

1.3 Building a Prototype

When the cooperation with Mr. Guzzinati ended without anything being designed or built, I took over the project, at Mr. Speroni's[1] invitation, and started designing a prototype of a composite carriage that could replace the steel one. Initially the design was to ignore the thermal deformation problem. The work was done at Speroni. We were provided of all the information pertaining to the carriage: geometry, loading, constraints, deformations requirements, and the preliminary design of the carriage drawn by Mr. Guzzinati. During this period I was joined by Paolo Barbieri, a chemical engineer, who helped in the manufacturing phase, and later carried

---

[1] Mr. Giuseppe Speroni is the owner and the general manager of the homonymous company.

out all tests on the carriage, once it was mounted on the machine.

Three different designs of different levels of complexity were made for the carriage. We discussed these with companies that could build the carriage, and these discussions led to changes in the design, and to the choice of the company to build the carriage.

When the final design was taken to the contractor, Monfrini S.p.A. of Vanzaghello, Milano, we were permitted to go to their plant and follow the manufacturing process. We observed the different manufacturing techniques, and learned about some of the more commonly used materials. We also had the opportunity to talk with their designers, and discuss possible improvements of the design, that would help in mass production.

After the carriage was delivered, it was taken to Speroni for the metalworking needed to prepare housing for the mechanical parts and to mount the carriage on the machine. Several standard tests were conducted on the carriage, including some simple static and dynamic test.

1.4 Testing the Prototype

The prototypal carriage was mounted on one of the machines to verify its overall layout as, for instance, position of the attachments and overall dimensions, and to check its response when the preload of the bearings was applied, and the carriage was moved on the tower. Next a straightness test of the Z axis[2], identified by the direction of motion of the carriage on the tower, was performed. An optical lens was mounted on the carriage in place of the

---

[2] The machine has an internal coordinate system which is identified by the direction of motion of the slide on the base, X axis, of the tower on the slide, Y axis, and of the carriage on the tower, Z axis.

sensor. A laser beam, generated at the base of the tower, pointing upward, reflects in the lens and returns back down into an optical device that determines its position in the X-Y plane. Theoretically the beam should hit the same point in the X-Y plane no matter where the carriage is on the tower. In fact due to imperfection of the machine, as the carriage moves along the tower, the beam hits the optical device at many different positions. The deviations from the nominal position of the hitting point along the X and the Y axes, are recorded while the carriage is moved up and down on the tower. Measurements are made for the X and the Y axes separately, over five runs of the carriage up and down the tower. The mean value of the error gives information on the straightness of the tower, while the standard deviation, measures the repeatability of the path of the hitting point, and is mainly caused by the response of the carriage to the dynamic loads associated with the motion. In the majority of the tests, a small value of the standard deviation was recorded, indicating a good behavior of the prototype.

A couple of very simple loading tests were also made on the carriage to verify its response to loading acting for long periods of time, and to check whether the carriage sustained any permanent deformations. Tests showed that the deformations vanished when the load was removed and did not change when the load was kept acting on the structure for long periods of time.

The weight of the composite structure alone was approximately 65N. About 60N of metal parts and 30N of bearing slides were added to it for a total weight of around 155N , vs. more than 1000N of the steel carriage. The result is really promising if we consider that the weight of the metal parts is about as much as the composite, and most of them can certainly be redesigned for a smaller weight, and some may be even removed. The weight of the composite structure may be also reduced, if built with a mold, taking the total weight below 100N.

1.5 The Speroni's Inspection Robot

Many different kinds of CMMs can be found on the market [2] , ranging in price from \$50,000 to \$75,000 for average performance, up to \$200,000 to \$500,000 for high-end machines, with accuracy below one micron in controlled lab environments. CMMs are divided in two main groups, according with the layout of their structure: bridge design machines, and cantilevered arm machines. With high stiffness and great stability, bridge machines are used for high precision measurement, while cantilevered arm machines are generally used for on-line automated inspection. However, at present, many of the best horizontal arm machines outperform average bridge CMMs, and approach the micron precision.

Speroni's machines belong to the second group, and have been chosen by famous companies worldwide, mainly for on-line inspection. The most common layout of a Speroni's touch-based inspection robot, and in general of a cantilevered CMM, is shown in Fig. 1.1. The robot has three main axes of movement, that correspond, respectively, to the movements of the slide, the tower, and the carriage. The sensor is rigidly fixed on the carriage. Three magnetic encoders, or scales, give the relative position of the slide with respect to the base, of the tower with respect to the slide and of the carriage with respect to the tower. Together these fix the spatial position of the sensor. A fourth axis may be represented by a rotating table housing the inspected component. The three parts and the table are moved by four electric motors, one per axis. The 3-D position of the sensor, and consequently the coordinates of the touched point, is measured with a precision ranging from one to ten micron.

The robot is controlled by a computer through a program called *path program*, which is basically a list of operations that the robot has to do in order to move and to measure coordinates of a particular piece. For example a path program to measure the coordinates of an isolated point could be:

1 - start the machine;
2 - move it along the three axes, at a speed of 500 mm/sec (called moving speed), until it gets close to the point;
3 - reduce the speed to 10 mm/sec (called measure speed), until the sensor touches the surface of the piece;
4 - read the coordinates on the scales;
5 - start again to the next point.

The path program is generally prepared by manually performing the movements needed to measure a particular object and recording them step by step in a suitable machine language. Once all operations are done, the program is launched and the machine repeats them one by one, measuring similar pieces.

The maximum acceleration of the present Speroni's machine with steel structure is limited to 250 mm/sec^2. Higher accelerations may cause problems in the mechanical transmission, and generate vibrations of the structure, disrupting the regularity of the motion of the machine. The sensor measures the coordinates of a point only when the vibrations are below a fixed threshold. A higher deceleration may cause the machine to stop and wait until all oscillations are damped out before reading the scales.

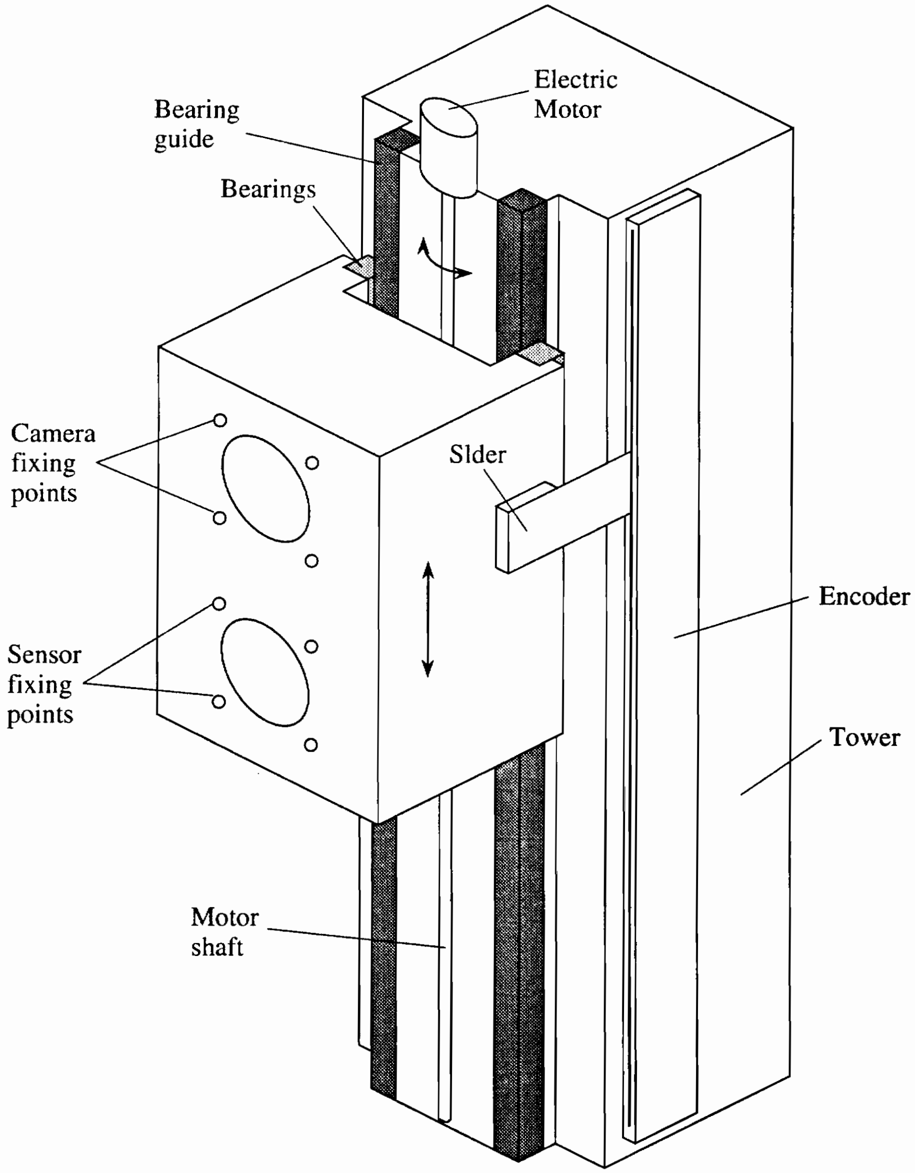

Figure 1.2 - General layout of the carriage and the tower.

The carriage, Fig. 1.2, is a very stiff structure moving on the tower, along the machine vertical (z) axis. The carriage is fixed to the tower by means of four bearing slides, allowing it to move only along that axis. To prevent rolling and pitching of the carriage during its motion, the bearing slides are forced towards the corresponding bearing guides on the tower by a preload force of 1200 N.

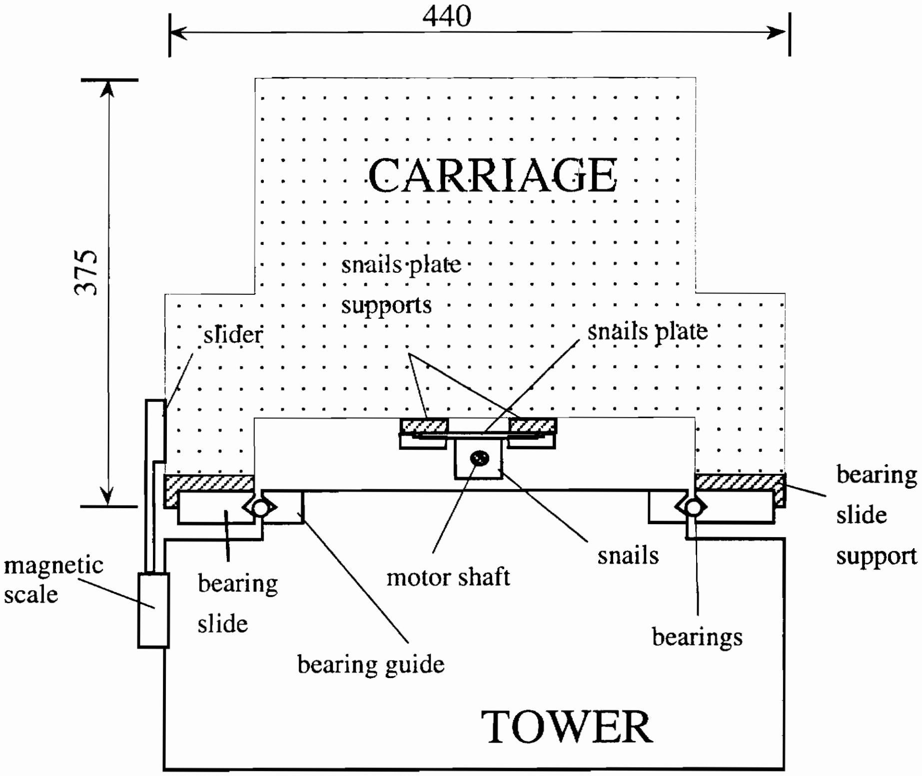

Figure 1.3 - Carriage layout; top view with principal components.

The carriage is moved by a number of linear actuators, Fig. 1.3, also called snails, because, like snails, they slide on a vertical bar when it is rotated by the motor. The number of actuators depends on the mass of the carriage, and on the given acceleration. The snails are fixed on a metallic thin plate, which in turn is bolted to the back plate of the carriage. The position of the carriage with respect to the tower is measured by one of the encoders, fixed on the tower, that reads the position of a slider fixed on one side of the carriage. On the front of the carriage, Fig. 1.4, we find the fixing

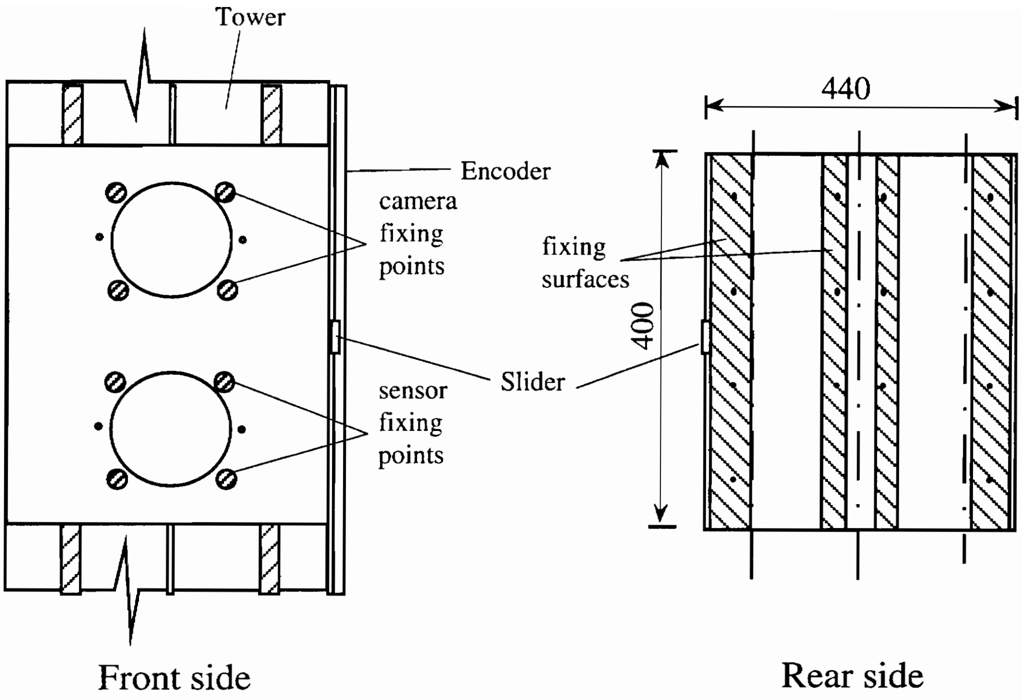

Figure 1.4 - Carriage front and rear view.

points for the sensor and for an optional second sensor or for a camera. On the rear side are located the surfaces where the bearings and the linear actuators are attached to the carriage. These surfaces are made with precision metalworking to meet strict tolerances on their position and their planarity.

2 Design of the Carriage

2.1 Design Requirements

When we started considering possible configurations for the carriage, we realized that the most stringent requirements were the small amount of time we had, and the budget we were given. For these reasons we decided to avoid a structure that would require a mold, and to employ instead simple components, mainly plates, that could be bonded together with structural adhesives.

As a replacement for the present steel carriage the composite carriage had to satisfy the following requirements:

1 have similar structural performance, i.e., have similar value of deflections under the same set of loading;

2 - be compatible with old movement hardware. In the back side of the carriage we had to provide supports for the bearings and for the plate carrying the actuators. The surfaces of these supports had to meet stringent requirements on their planarity and their position, obtainable only through precision metalworking;

3 - provide attachments for the sensor and camera, in the front side of the carriage, whose surfaces had to meet the same requirements of point 2;

4 - provide room for the secondary machine hardware (slider, controls, electronics);

5 - weigh much less than the steel carriage. Based on previous experience, and on estimates made by Mr. Guzzinati, our target was around 100N

for the bare structure, compared to the about 1000 N of the steel carriage.

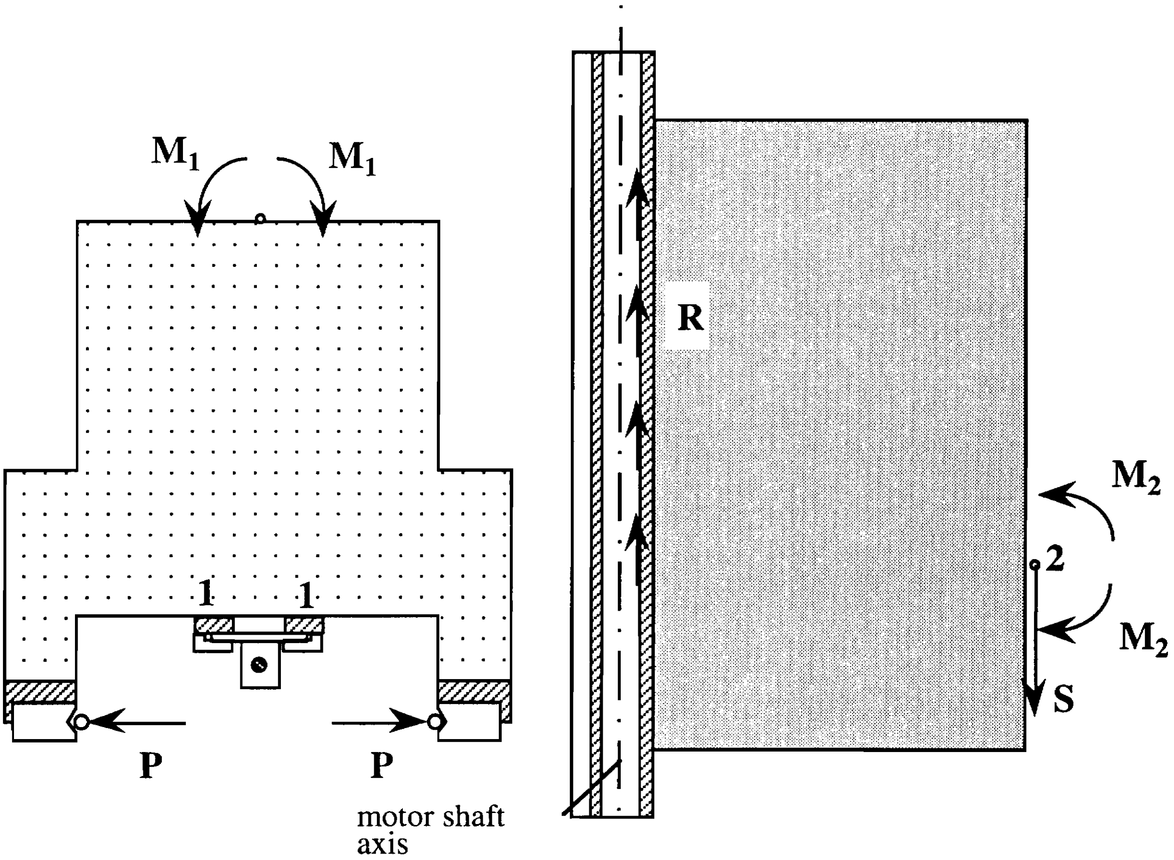

Figure 2.1 - Carriage loading.

The carriage is loaded by three groups of loads, shown in Fig. 2.1.

1 - The preload **P** on the bearings acting along the y direction and pointing outwards is applied on the bearing supports. The preload is eccentric with respect to the carriage center of mass, generating bending moment. Although the composite carriage would be much lighter than the steel one, and need a smaller preload force to prevent unwanted movements, we were asked to consider the value of the preload used for the latter, **P**=1200N.

2 - The weight **S** of the measuring equipment, is considered concentrated at the sensor fixing points, in the front of the carriage, and equally divided among them. Dynamic loads generated by the motion of the carriage, are considered through static equivalent loads, accounting for the weight of the measuring equipment, and the inertia forces caused by the acceleration along the y and the z axes, positive or negative according to the direction of the movement on this axis. Due to the eccentricity with respect to the center of mass of the carriage, these loads generate moments $\mathbf{M_1}$ and $\mathbf{M_2}$ about the Z and Y axes, respectively. The value of the force **S** and the moments $\mathbf{M_1}$ and $\mathbf{M_2}$ has been specified by Speroni as $\mathbf{S} = 200\text{N}$, divided into $\mathbf{S_1}$ and $\mathbf{S_2} = 100\text{N}$, and $\mathbf{M_1} = \mathbf{M_2} = 40\text{Nm}$.

3 - The force transmitted by the linear actuators **R**, acting along the Z direction, and applied on the snail supports on the back side of the carriage. In the present analysis, **R** is considered a reaction force, and thus is not fixed a priori.

Even though the magnitudes of the loads were quite small, we had to consider very stringent requirements on the deformation of the carriage: the deflection at the linear actuator support points, marked **1** in Fig. 2.1, had to be kept as low as possible, and we fixed a target value of ten microns. The displacement of the structure in the Z direction, at the sensor fixing points, marked **2** in Fig. 2.1, had to be within four microns. These limits required the design of a very stiff structure.

2.2 Candidate Designs

From a structural point of view, we identified two main functions:

1 - resist the preload forces and minimize bending of the structure about the Z axis to minimize the displacements of the points where the snails plate is bolted to the carriage;

2 - minimize relative displacements between the attachments points for the sensor and the slider by which we identify the position of the measured point.

According to these two functions we decided to make the carriage from two substructures, Fig. 2.2, one that we called support, on which the sensor was mounted, and a second that we called interface, connecting the support to the tower of the machine, and carrying the hardware necessary for its

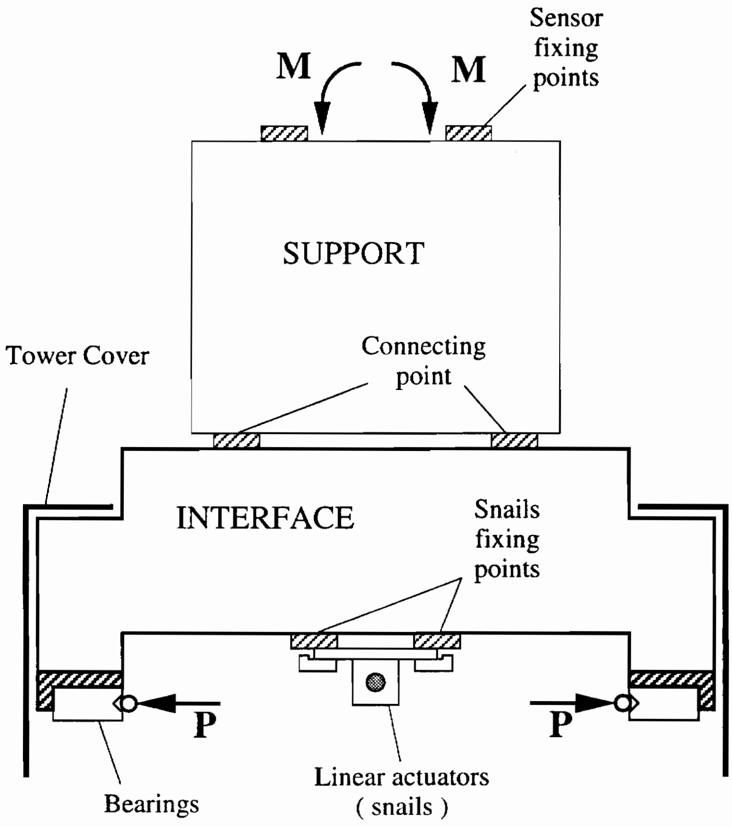

Figure 2.2 - General layout of the proposed design.

motion (bearings and actuators plate). This division would permit Speroni to change the support to fit particular applications, without changing most of the carriage. The front side of the interface would exit from the cover of the tower, so that maintenance on the measurement equipment or replacement of the support could be done without removing the cover, and independently from the rest of the machine. Finally we decided that the bearing slides should be fixed from the front side of the carriage, rather than from the back as it was for the old carriage, to make maintenance easier.

We decided to make the structure out of sandwich panels rather than solid laminates, since higher values of stiffness for the same weight can be reached with the former. To allow doing the necessary precision metalworking on the support surfaces, itemized at points 2 and 3 of the design requirements at the beginning of the chapter, we used stainless steel discs, bonded to the composite. Our lack of experience with the strength of bonded joints suggested to make the discs with a small cylinder, that passed through the core of the sandwich and was bolted to the panel with a similar second disc. It certainly was not the lightest solution but it gave us enough

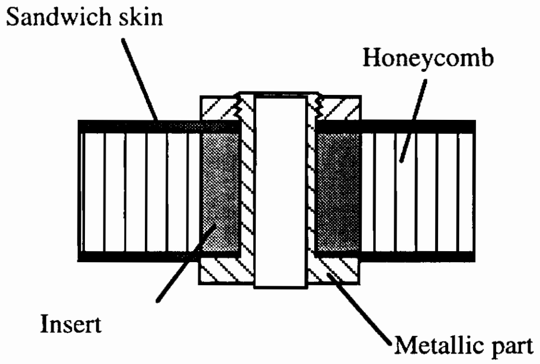

Figure 2.3 - Detail of the reinforcement for sandwich plates, and the metal discs used to provide attaching surfaces for the machine hardware.

confidence about its strength. One of the design requirements for sandwich panels is that the core should have sufficient compressive strength to withstand out of plane loads acting on the skins. To prevent local failure mode at points where the metallic parts were attached to the composite, we reinforced the sandwich with inserts, replacing the honeycomb, and connecting the two skins, as shown in Fig 2.3.

As previously mentioned, we defined three possible designs for the interface and a common one for the support. For the interface, the three different solutions, labeled A, B, and C are described below.

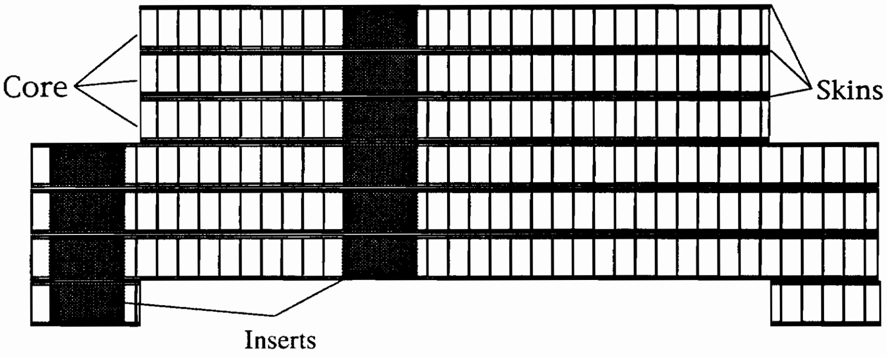

Figure 2.4 - Horizontal cross section of Design A.

Design A, in Fig. 2.4, was made of six 20 mm sandwich plates, attached with structural adhesive. This design was certainly the simplest of the three, the fastest to be built, since the plates could be attached without using special tools or machines, thus the cheapest in terms of cost of manufacturing. However it was heavier than the other designs, since it was a full volume, it was more expensive in terms of material used, and did not allow easy positioning of the several attachment points. The inserts, Fig. 2.3, should have replaced the core of many layers of sandwich in all points where reinforcement was needed, and the many metallic parts should have been quite large and heavy. Finally, the experience derived from building it would not help in the design of more difficult structures.

Design B, shown in Fig. 2.5, was made up of a main plate and a big C section attached to it. Part of the outer skin of the C wraps around the main plate to provide some continuity of the fibers. Two horizontal stiffeners are located inside the C section to increase the bending stiffness of the structure, and better resist preload forces. This design was the lightest, and it was structurally sound, because it was virtually made out of a single piece, and it had fibers continuous all around it, giving it good bending stiffness. It was quite easy to manufacture, but it required a mold for the C section, and again did not easily allow positioning of some inserts in the panels because of the laterally inclined surfaces.

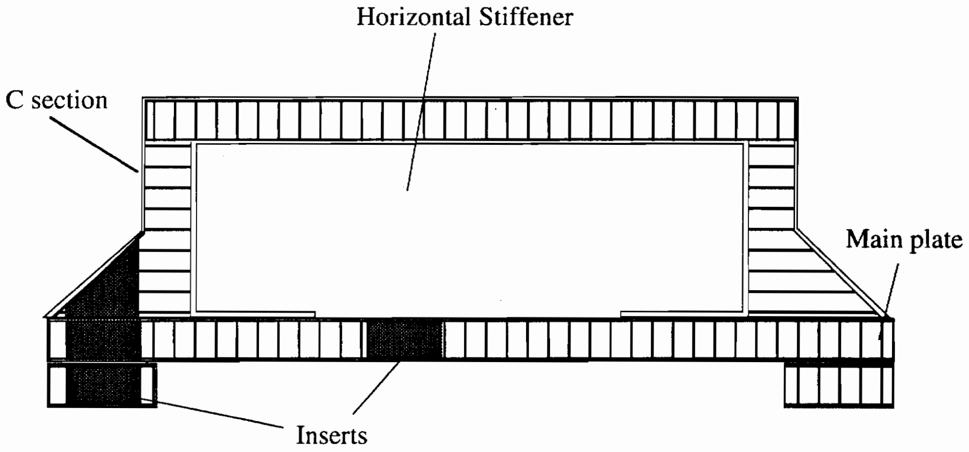

Figure 2.5 - Horizontal cross section of Design B.

Design C, Fig. 2.6, was similar to B, but it allowed for easy positioning of the inserts, and did not need a mold since it was made by assembling simple parts. The C section was replaced with three separate plates, and the two horizontal stiffeners inside the C were now running from one side to the other of the main plate, passing through the flanges of the C. The price paid was a little lower stiffness due to the structural joining.

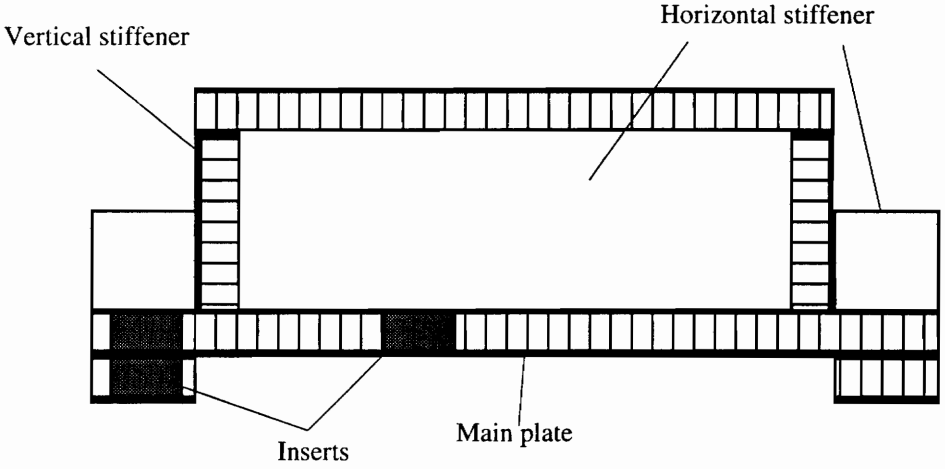

Figure 2.6 - Horizontal cross section of Design C.

Design C satisfied best all requirements, being easy enough to make by the due date, allowing good control of all manufacturing phases, and representing, thanks to the various kinds of procedures needed, good experience towards future designs. However, for mass production, design C could not guarantee good repeatability, due to the additional work required to assemble it. Also, every piece would have suffered the high cost of assembly. For mass production, design B was to be preferred to design C, providing the problem of inserting the panels was solved.

The structure of the support was made in the same way of design C of the interface, with two main plates connected by a framework of horizontal and vertical stiffeners. As for the interface, the design will have to be reconsidered in case of mass production, in favor of structure with lower assembly cost.

2.3 Detail Design

A more detailed picture of the interface according to the design C and of the support is shown in Fig. 2.7. As mentioned before, the interface was mainly subject to bending and axial loads by the preload forces of the bearings.

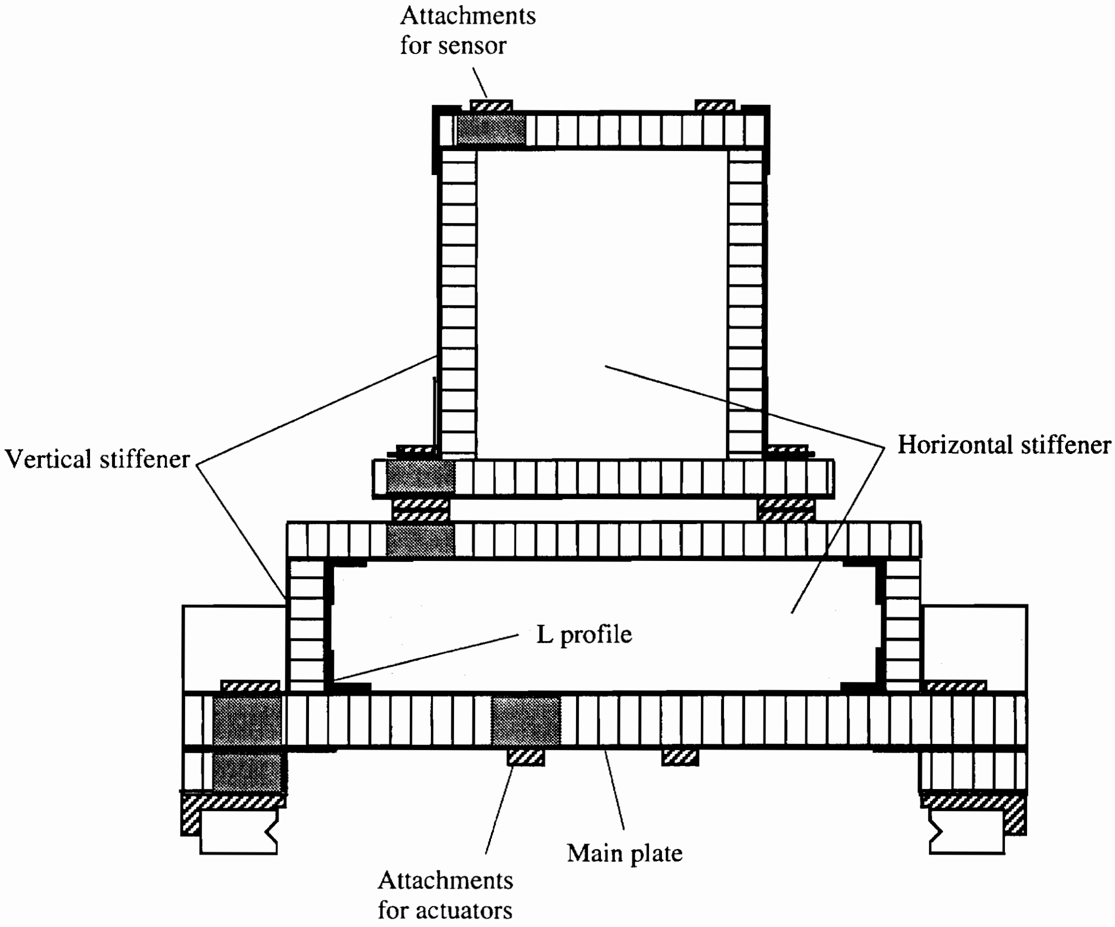

Figure 2.7 - Horizontal cross section of the interface and the support: final design.

Because of the limit on the midspan deflection, the bending moment, although quite small in magnitude, was the critical load for this part of the structure. To provide the interface with the necessary bending stiffness, we decided to construct it from two main sandwich plates linked together by a framework of horizontal and vertical stiffeners, and two supports for the bearing slides, also made from sandwich structure. Several L shaped laminate profiles where used to reinforce the connections between the panels. In this way the two main plates worked as the flanges of an I profile, giving good bending stiffness. The thickness of the back plate, which directly carried the bearing load, was 30 mm, and the thickness of the other plates was 20 mm.

The plate skins were symmetric and balanced four-ply laminates. The stacking sequences, shown in Fig. 2.8, were different for the main plates of the interface and for all other plates. For the main plates of the interface, the stacking sequence had two 0°/90° woven plies on the outside of the laminate and two unidirectional 0° plies in the inside, to provide good bending and in plane stiffness, while for all other plates the two unidirectional plies were replaced with two ±45° woven plies, to provide good shear stiffness. Overall we then had three different lay-ups for the panels. This certainly will have to be improved, reducing the number of different panels, to reduce manufacturing costs. The plates were built separately and bonded with structural adhesive, reinforcing the joints with carbon fiber L profiles, Fig.

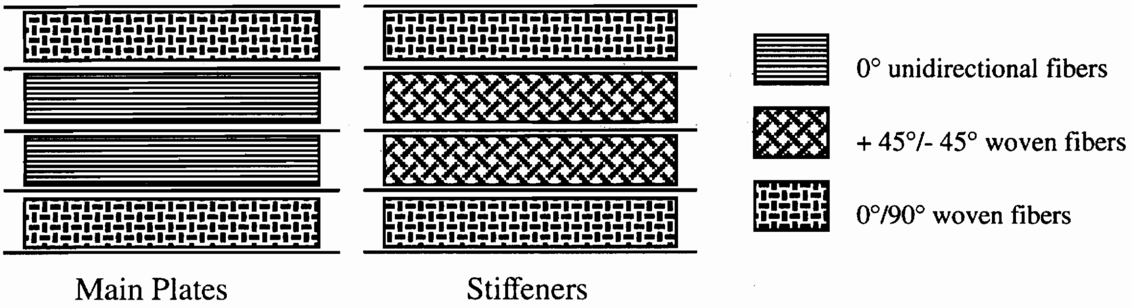

Figure 2.8 - Stacking sequences for the sandwich skins.

2.7. As mentioned above, at all the points where the metal parts were to be attached, the panels were reinforced by locally replacing the honeycomb core with inserts, thus providing great resistance to out-of-plane loads, and avoiding local failure of the sandwich.

Table 2.1 - Material properties.

	E_1	E_2	G_{12}	ν_{12}	G_{1Z}	G_{2Z}	t	ρ
Units	N/mm2				N/mm2		mm	N/mm3
UD	$133.5\ 10^3$	$8.73\ 10^3$	$4.41\ 10^3$	0.304	--	--	0.125	$1.546\ 10^{-5}$
Fabric	61.130^3	$61.13\ 10^3$	$4.10\ 10^{3‡}$	0.04‡	--	--	0.31	$1.617\ 10^{-5}$
Honeycomb	6.0* 6.0*	6.0* 6.0*	4.41* 4.41*	0.3* 0.3*	26.21 41.388	10.35 20.0	28.6 14.3	$0.283\ 10^{-6}$ $0.534\ 10^{-6}$
	X Tensile Strength	Y Tensile Strength	Shear Strength					
UD	1891.7	75.1						
Fabric	904.5	904.5						
Adhesive			3.5					
UD	Cycom 759 GT2 130 by American Cyanamid Co. [3]							
Fabric	Cycom 759 Fabric by American Cyanamid Co. [3]							
Honeycomb	HRH-10 1/16-3.4 and HRH-10 1/8-1.8 Hexagonal cell by Excel Co. [4]							
Adhesive	Redux 410 paste adhesive by Ciba-Geigy [5]							

Properties are taken from data sheets provided by the above companies except:
‡ Properties of similar materials taken from [6]
* Properties assumed by the author

2.4 Simple Estimate of Stresses and Displacements

As previously mentioned, the stresses associated with the loads were not critical, and the main constraint were prescribed displacements of some particular points of the carriage. The properties of materials used for the construction of the structure are given in Table 2.1. The stresses and displacements were first calculated using simple strength-of-materials approach.

The loads that we considered for the support and the interface are shown in Figs. 2.19 and 2.10, respectively. For the support we only considered the front loads $S_1=S_2=100N$, and the moment about the Y axis $M_2=40000Nmm$, disregarding the moment M_1 about the Z axis.

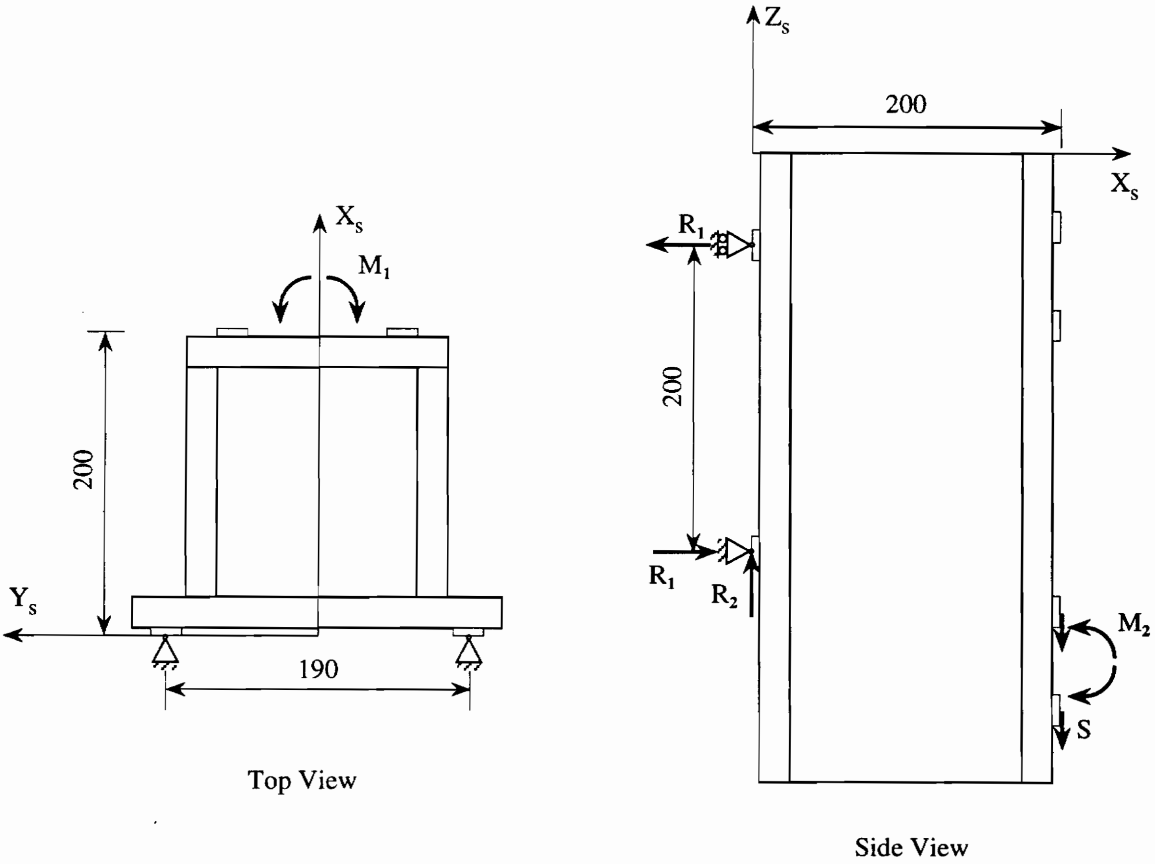

Top View

Side View

Figure 2.9 - Support geometry and loading (dimensions in mm).

For the interface, for the sake of simplicity, we considered the moment $M_3=200R_1$ instead of the reaction forces R_1 coming from the support.

$\mathbf{M}_l$=80000Nmm, and **T**= 200N act on the front side, and the bearing preload forces **P**=1200N on the back side. The weight of the structure was neglected.

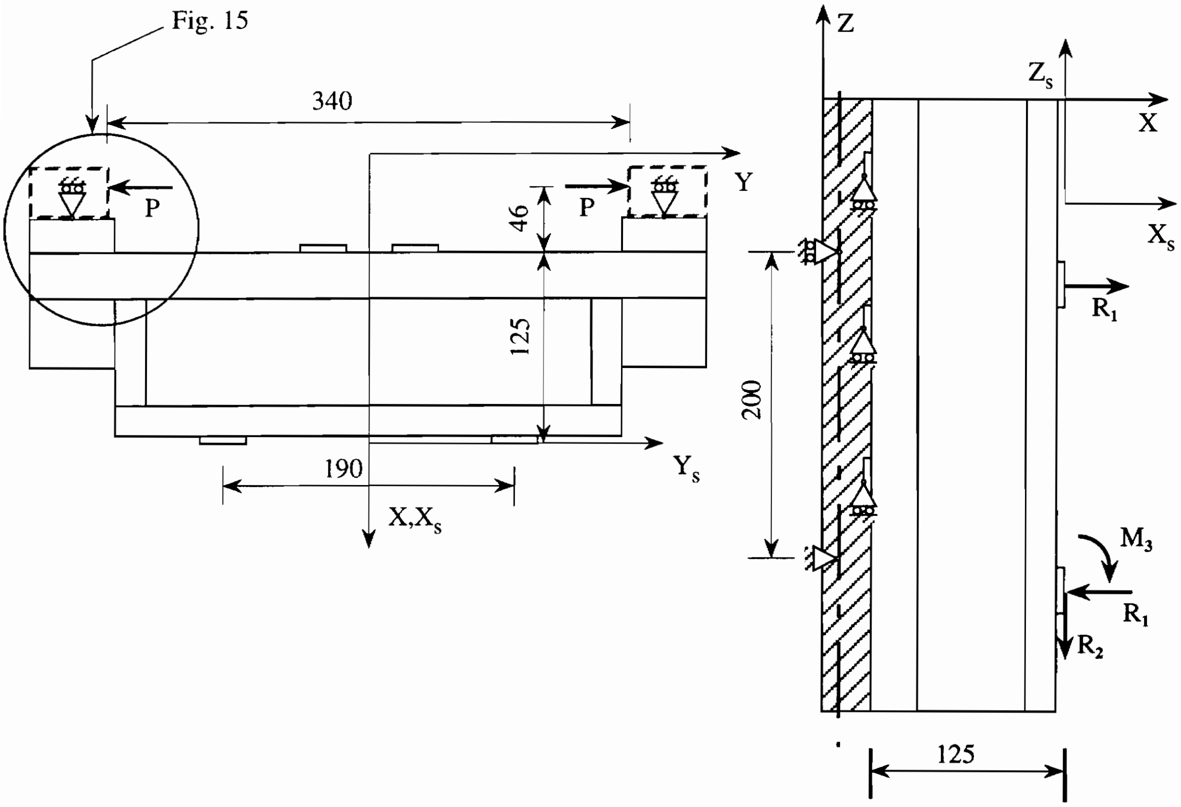

Figure 2.10 - Interface geometry and loading (dimensions in mm).

We first calculated the stresses in the attachment surface between the bearing support and the back main plate, Fig 2.11.

The composite bearing support is attached to the main plate with structural adhesive. The bearing preload force **P**=1200N is transmitted from the bearing composite support to the main plate through this surface, having an area of A = 42000mm^2. Assuming a uniform stress distribution over the surface, we obtain the transmitted shear stress to compare with the shear strength of the adhesive:

$$(2.1) \qquad \tau = \frac{P}{A} = \frac{1200}{42000} = 0.03\text{N/mm}^2 < 3.5\text{N/mm}^2$$

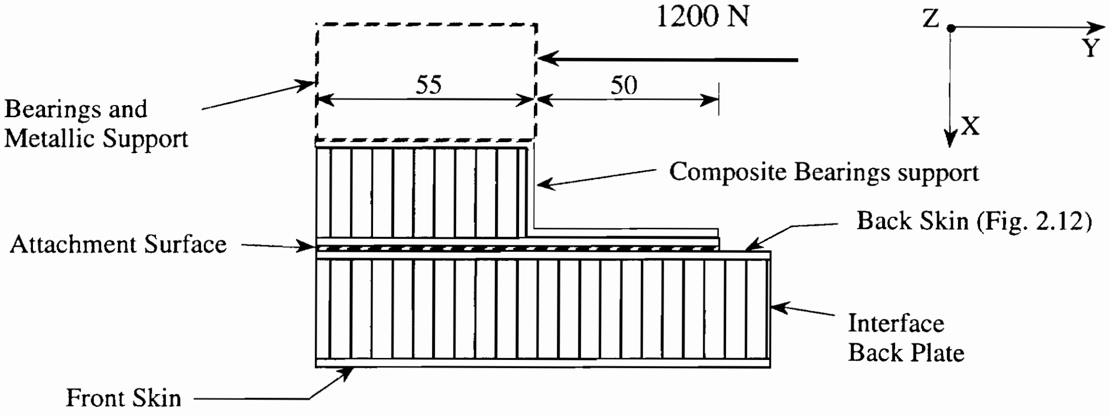

Figure 2.11 - Attachment surface between main back plate and bearing support.

Next we considered the elongation and the stresses in the back skin of the interface back panel, Fig. 2.11, where the composite bearing supports are attached. Figure 2.12 shows the geometry and the loading of the considered laminate skin.

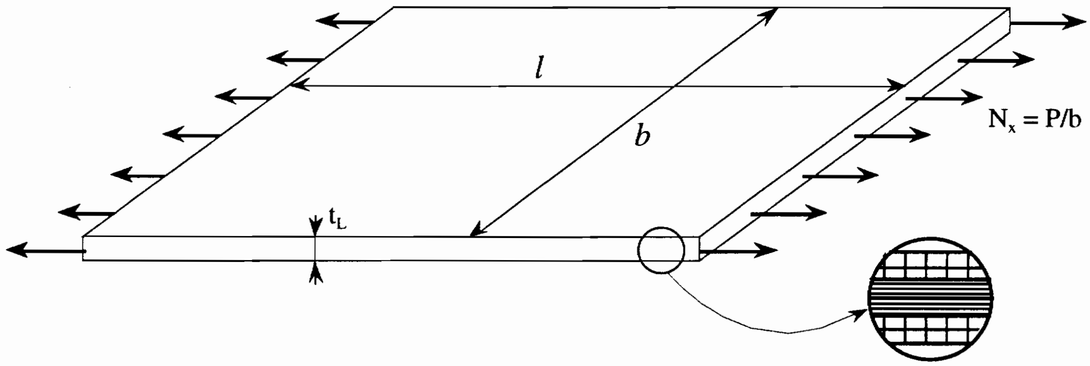

Figure 2.12 - Loading and geometry of the back skin of the main panel.

To be conservative we assumed that the entire preload force **P** was carried by this skin. The stacking sequence of the laminate was $((0/90),0)_S$, see also Fig. 2.8, where (0/90) represents the woven plies with fibers oriented at 0° and 90° angles. Properties and thicknesses for the two different plies are given in Table 2.1 .

The total thickness of the laminate is $t_L = 0.87\text{mm}$. To obtain the elongation of the skin we have to calculate the inverse of the in plane stiffness matrix of the laminate [A]. According to the Classical Lamination Theory [7], the matrix is:

$$(2.2) \qquad [A]=\begin{bmatrix} 71539 & 2186 & 0 \\ 2186 & 40157 & 0 \\ 0 & 0 & 3645 \end{bmatrix}$$

Using the relation

$$(2.3) \qquad \{N\}=[A]\{\boldsymbol{\varepsilon}\}$$

we obtain

$$(2.4) \qquad \{\boldsymbol{\varepsilon}\}=[A]^{-1}\{N\}=[\overline{A}]\{N\}$$

and the elongation is then:

$$(2.5) \qquad \boldsymbol{\varepsilon}_x=\overline{A}(1,1)N_x=\overline{A}(1,1)\frac{P}{b}=0.14002\cdot 10^{-4}\frac{1200}{400}=0.4201\cdot 10^{-4}$$

$$(2.6) \qquad \boldsymbol{\varepsilon}_y=\overline{A}(2,1)N_x=\overline{A}(2,1)\frac{P}{b}=-0.00762\cdot 10^{-4}\frac{1200}{400}=-0.0229\cdot 10^{-4}$$

The stresses in the plies can now be calculated as:

$$(2.7) \qquad \{\boldsymbol{\sigma}\}^{(i)}=[Q]^{(i)}\{\boldsymbol{\varepsilon}\} \qquad\qquad \boldsymbol{\sigma}_x^{(i)}=Q^{(i)}(1,1)\boldsymbol{\varepsilon}_x+Q^{(i)}(1,2)\boldsymbol{\varepsilon}_y$$

where $[Q]^{(i)}$ is the reduced stiffness matrix of the i^{th} ply.

The stresses in the plies of the laminate are:

$$(2.8) \qquad \boldsymbol{\sigma}_x^{(UD)}=134310\cdot 0.4201\cdot 10^{-4}-2670.1\cdot 0.0229\cdot 10^{-4}=5.64\text{N}/\text{mm}^2$$

$$(2.9) \qquad \boldsymbol{\sigma}_x^{(Fabric)}=61228\cdot 0.4201\cdot 10^{-4}-2449.1\cdot 0.0229\cdot 10^{-4}=2.57\text{N}/\text{mm}^2$$

which are far below the allowable values for the material.

Next we evaluated the displacements of the carriage at points where they were constrained. For the following calculation we used equivalent laminate properties that can be obtained from the in-plane stiffness matrix of the laminate [A]. The [A] matrices for the skins of the front and the back plates of the interface $[A]^I$, and for the skins of all other plates $[A]^S$, Fig 2.8, are respectively

$$(2.10)\qquad [A]^I = \begin{bmatrix} 71539 & 2186 & 0 \\ 2186 & 40157 & 0 \\ 0 & 0 & 3645 \end{bmatrix} \qquad [A]^S = \begin{bmatrix} 60243 & 18716 & 0 \\ 18716 & 60243 & 0 \\ 0 & 0 & 20763 \end{bmatrix}$$

Using the relation

$$(2.11)\qquad \{N\} = [A]\{\varepsilon\}$$

we can obtain the strain vector

$$(2.12)\qquad \{\varepsilon\} = [A]^{-1}\{N\} = [A]^{-1}\{\sigma\}_L t_L = [S]_L\{\sigma\}_L$$

where $[S]_L$ represent a sort of laminate reduced compliance matrix, from which we can obtain the laminate stiffness properties.

$$(2.13)\qquad E_1^L = \frac{1}{S_L(1,1)}; \qquad E_2^L = \frac{1}{S_L(2,2)}; \qquad G^L = \frac{1}{S_L(3,3)}; \qquad \nu_{12}^L = -\frac{S_L(1,2)}{S_L(1,1)}$$

In many cases these properties can be used with sufficient accuracy to evaluate the response of the laminate. For these laminates the approximate properties are presented in Table 2.2.

We considered the deflection of the interface at mid span, caused by the moment given by the offset of the preload forces Fig. 2.13. To calculate the deflection we assumed that the two plates are rigidly linked by the stiffeners,

Table 2.2 - Approximate properties for the composite laminate skins.

Units=N/mm^2	E_1^L	E_2^L	G^L	v_{12}^L
Main plates	82092	46081	4189.1	0.0544
All others	43894	43894	16745	0.311

and they work as flanges of an I profile, and in each plate we further assumed that only the skins resist to the loads. We considered the honeycomb having infinite shear modulus and neglected plate effects.

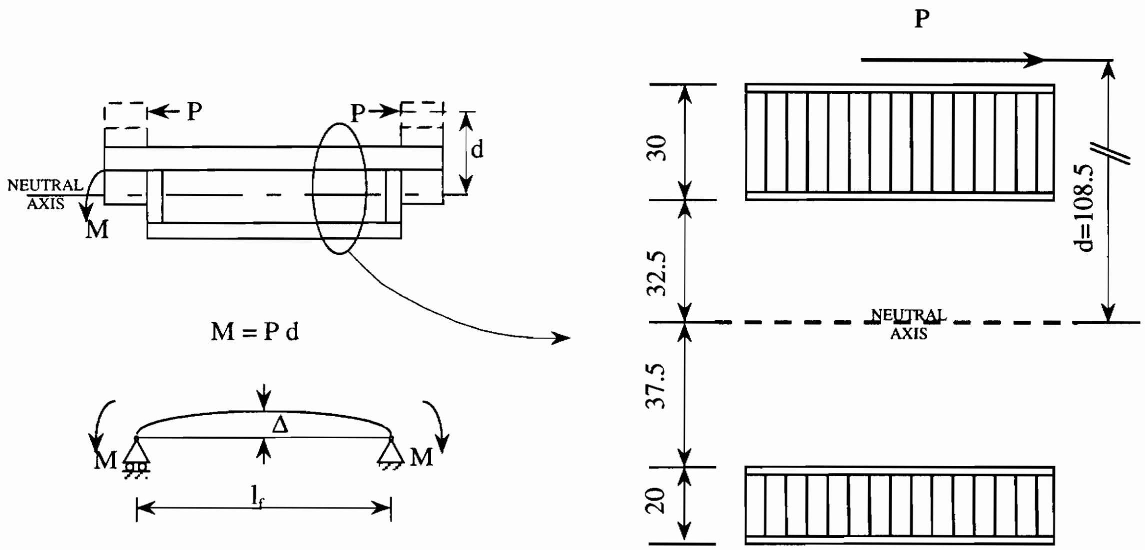

Figure 2.13 - Dimensions and loads of the interface.

The mid span deflection of the structure is then given by:

$$\Delta = \frac{1}{8}\frac{M}{E_1^L I} l_f^2 \tag{2.14}$$

where I is the moment of inertia of the skins with respect to the neutral axis of the interface, and l_f is the span of the interface, here considered to be the distance between the bearings, i.e. the points of application of preload forces $l_f = 340\text{mm}$. The value of the deflection is

$$\Delta = \frac{1}{8}\frac{130728}{82092 \cdot 3396407.8944}340^2 = 6.775 \cdot 10^{-3}\text{mm} \tag{2.15}$$

Last we checked the deflection in the z direction at the sensor attachment points. The total deflection is assumed to be given by the sum of the deflections of the support and the interface considered as cantilevered beams. Each one of them is the sum of the deflection due to bending and the deflection due to shear, which are given as:

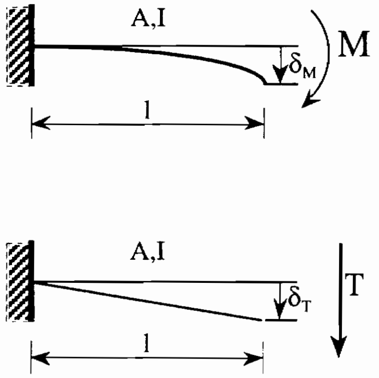

$$\delta_M = \frac{Ml^2}{2EI}$$

$$\delta_T = \frac{2T}{AG} + \frac{Tl^3}{3EI}$$

Figure 2.14 - Bending and shear deflection of a cantilevered beam.

The area A and the moment of inertia I are calculated considering the y-z cross section of the skins of the stiffeners, and neglecting the contribution of the honeycomb core. We also neglected the deformation of the front and the back plates of the substructures.

The dimensions and layout of the panels of the interface are shown in Fig. 2.15., where because of symmetry considerations only the upper half is displayed. The resisting cross section, as can be seen in the front view, is

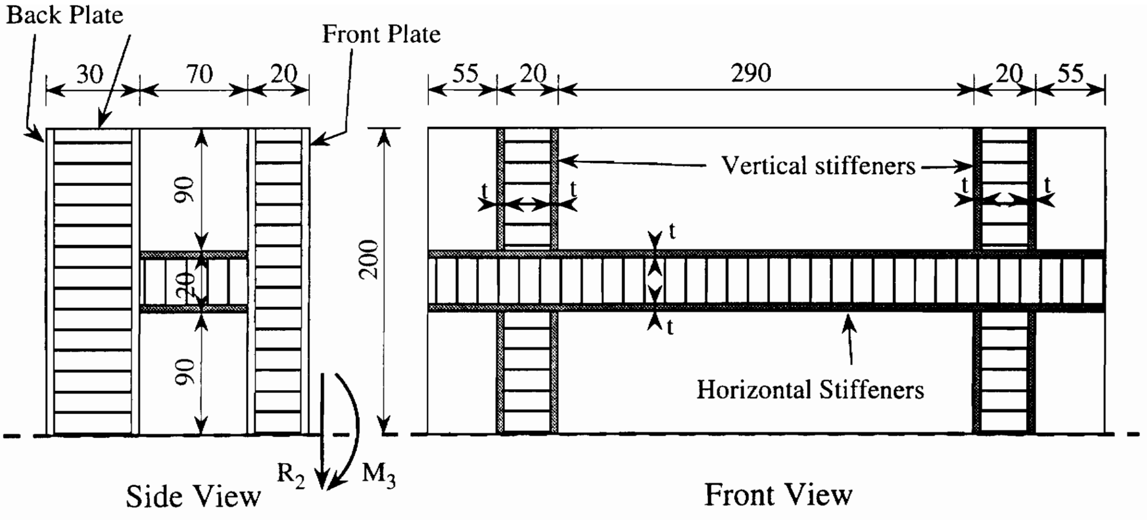

Figure 2.15 - Stiffeners layout of the interface (dimensions in mm).

given by the skins of the stiffeners, i.e., the panels between the front and the back plate. The contribution of the horizontal stiffeners is only considered for bending response, but neglected when considering the deflection due to shear. Since we only consider the deformation of the stiffeners, the length of the beam is given by the distance between the front and the back plate.

For the interface we have the following data, where A takes into account only the vertical stiffeners:

$t = 1.24mm$	$A = 1775.68mm^2$	$I = 46399791mm^4$
$l = 70mm$	$T = 200N$	$M = 80000Nmm$

and the resulting value of the deflections result in:

$\delta_M{}^I=9.6236\ 10^{-5}mm$ $\delta_T{}^I=4.8209\ 10^{-4}mm$

For the support, the geometry of the stiffeners is shown in Fig. 2.16, and we have the following values of the cross section properties:

$t = 1.24mm$	$A = 2033.6mm^2$	$I = 28528036mm^4$
$l = 160mm$	$T = 200N$	$M = 40000Nmm$

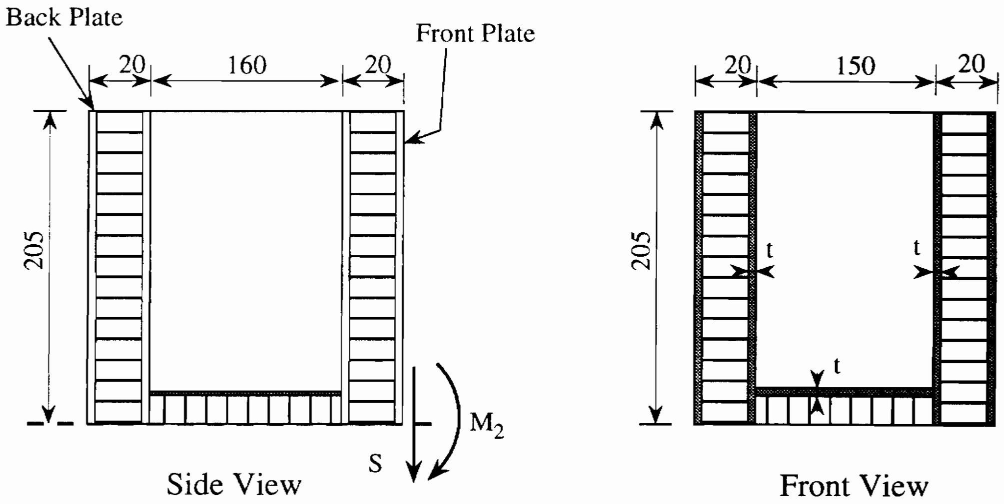

Figure 2.16 - Stiffeners layout of the support (dimensions in mm).

The resulting deflections are:

$\delta_M{}^S$=3.5937 10^{-4}mm $\delta_T{}^S$=1.0607 10^{-3}mm

The sum of the four deflections gives the displacement of the sensor in the z direction with respect to the bearings.

δ_{Tot} = 1.9984 10^{-3}mm

The calculated displacements are then both within the limits given by Speroni. It must be kept in mind however, that this is only a rough indication of the real deformation, and a finite element analysis is necessary to obtain more reliable results.

3 Finite Element Analysis of Design

3.1 Introduction

As mentioned earlier, the composite carriage that was built was only a prototype. We had no experience with the materials, nor with the use of these materials; we knew little about the technologies involved in the process of manufacturing structures with composites, and we were pressed for time. Our predictions for the behavior of the structure were based on common sense and on the simple calculations that were previously described. The first tests on the carriage gave impressively good results in terms of small deformations of the structure, and very good behavior with respect to thermal and dynamic loads.

These results, however, cannot bring us to consider this as the final design, but rather to conclude that we have to keep working in this direction towards the design of a cost effective composite replacement for the old steel carriage. Despite the uncertainties related to the use of a new and mostly unknown material, and a slightly higher cost, the composite carriage proved that it could outperform the steel one. The partial failure of Speroni's previous experience with the use of composites was in part due to a lack of a more accurate analysis than what is needed for structures made of steel. Finite element analysis can help us predict the behavior of the new composite structure and numerical optimization can allow us to exploit the possibilities given by these new materials.

Before starting the optimization of the carriage we needed to decide on the kind of finite elements we would use in modeling, and to check their accuracy. We also had to create a model for the carriage that was simple enough to limit the computational time but fine enough to guarantee acceptable accuracy.

3.2 Accuracy of Elements Used in the Analysis

The structure of the carriage is primarily composed of several sandwich panels, bonded with structural adhesive. Many metal parts have been added to the composite structure, to link the two substructures together, Fig. 3.1, and to provide interfaces between the composite panels and the mechanical components that need to be attached to them. Inserts are embedded in the core to provide local reinforcement, and avoid collapse of the honeycomb under transverse point loads. Plate elements were used to model the panels, and metal parts and inserts were initially ignored in the analysis.

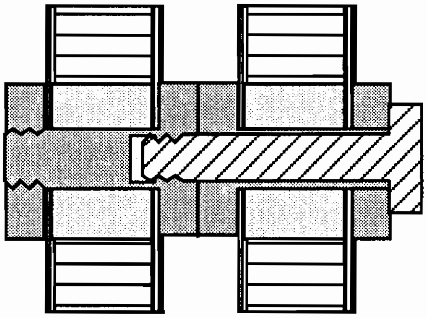

Figure 3.1 . - Detail of the joint between the two substructures.

Because the primary constraints for the structure were limits on displacements, we tried to determine what level of refinement in the mesh was needed in order to obtain accurate displacements. For this purpose we analyzed different simple plate problems, comparing the results with known solutions.

The first test case was a square, isotropic plate, clamped on all edges, and subject to a concentrated lateral load in the center, Fig. 3.2. The dimensions of the plate are $a = b = 20$ in and thickness $t = 1$ in. The aspect ratio $a/t = 20$ is similar to those of the panels of the carriage. The plate is made of aluminum for which we have $E = 10.92\ 10^6$ psi, and $\nu = 0.3$.

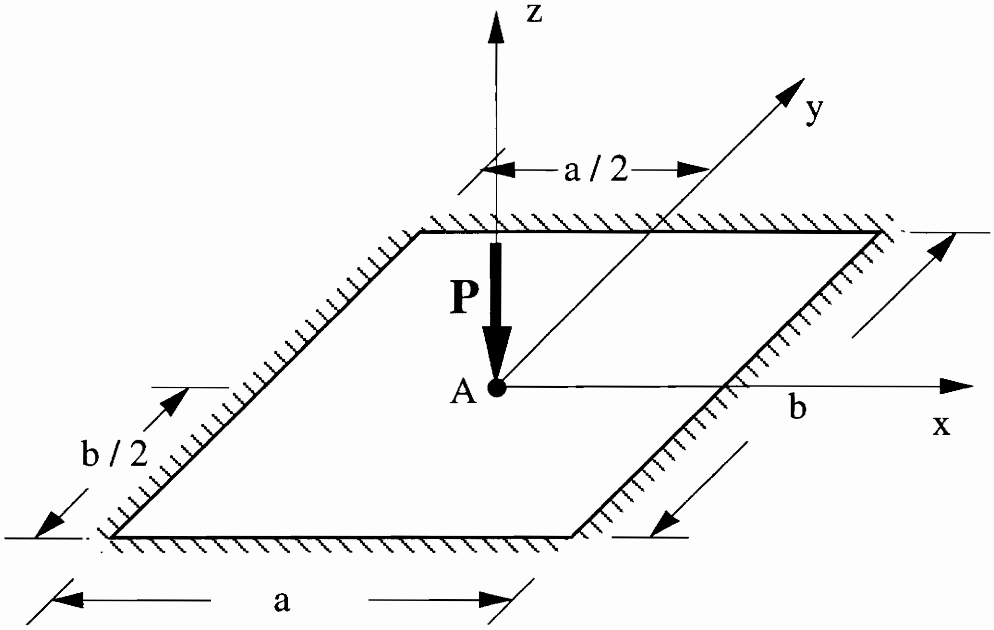

Figure 3.2 - Square isotropic clamped plate under point load.

The solution for this problem can be obtained using eq. 3.1 given by Timoshenko and Woinowsky-Krieger [8]:

$$\text{(3.1)}\qquad w = \frac{Pa^2}{2\pi^3 D} \sum_{m=1,3,5,\ldots}^{\infty} \frac{1}{m^3} \cos\frac{mpx}{a} \left[\left(\tanh\alpha_m - \frac{\alpha_m}{\cosh^2\alpha_m} \right) \right] \cosh\frac{mpy}{a}$$

$$-\sinh\frac{mpy}{a} - \frac{mpy}{a}\tanh\alpha_m \sinh\frac{mpy}{a} + \frac{mpy}{a}\cosh\frac{mpy}{a}$$

where

$$\alpha_m = \frac{m\pi b}{2a}$$

D is the flexural rigidity of the plate, and *m* and *n* are the number of halfwaves in the x and y direction respectively. Results were also compared with those obtained with a different finite element package, EAL [9]. Because of symmetry, only a quarter plate was analyzed, and different meshes were generated with both four and eight node plate elements.

Results for the Z displacement of the center node are shown in Table 3.1.

Table 3.1 - Center displacement (inches) for various models of square isotropic clamped plate.

unit = in	W_A	error %
Eq. 4.1	$- 8.97\ 10^{-3}$	--
EAL 64 E43	$- 8.960\ 10^{-3}$	0.11
NASTRAN 4 QUAD4	$- 8.375\ 10^{-3}$	6.63
NASTRAN 16 QUAD4	$- 9.060\ 10^{-3}$	1.00
NASTRAN 64 QUAD4	$- 9.059\ 10^{-3}$	0.99
NASTRAN 256 QUAD4	$- 9.010\ 10^{-3}$	0.44
NASTRAN 4 QUAD8	$- 8.688\ 10^{-3}$	3.14
NASTRAN 16 QUAD8	$- 8.941\ 10^{-2}$	0.32
NASTRAN 64 QUAD8	$- 8.972\ 10^{-2}$	0.02

The NASTRAN four-node element meshes show oscillating convergence towards the solution, but with 256 elements the error is still half a percent. With eight-node elements the convergence is monotonic and faster, and sixteen elements give already a quite accurate solution in terms of displacements. For the purpose of the present work, the approximation given by the four eight-node element mesh could be already considered sufficient.

It is interesting to point out, however, that four-node elements give a much better solution in terms of moments on the edge than eight-node elements. Fig. 3.3 shows the bending moment m_x on one of the clamped edges. Values for m_x are obtained using the formulas in [8], EAL and NASTRAN, using the two 64 node meshes. We can see that while EAL and the NASTRAN's four-node element mesh give results that are practically identical to those obtained analytically, the NASTRAN eight-node element mesh give values of the order of one third of the others.

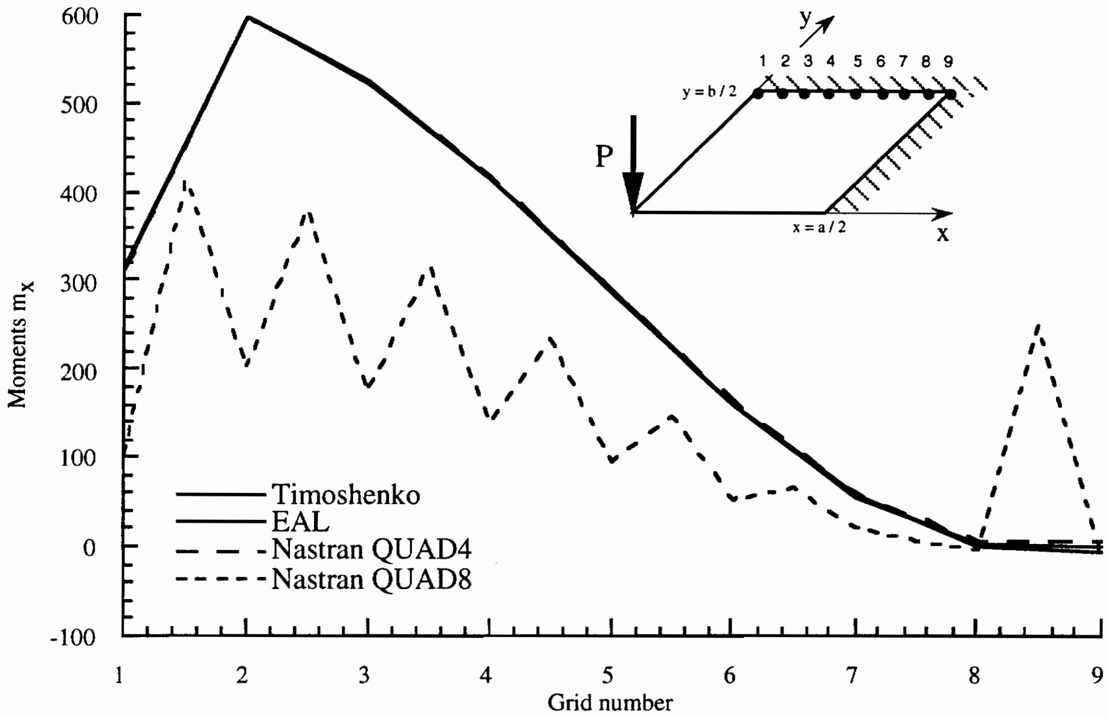

Figure 3.3 - Comparison of edge moments for isotropic clamped plate model.

The effects on the displacements of the transverse shear deformation can be very large for relatively thick plates (in this case a / t =20). Table 3.2 shows how the displacement in the center of the plate change if we introduce

Table 3.2 - Effects of transverse shear on center displacement (inches) of the isotropic plate models.

unit = in	W_A(no shear)	W_A(shear)	difference %
NASTRAN 4 QUAD8	$-8.688\ 10^{-3}$	$-9.487\ 10^{-3}$	9.20
NASTRAN 16 QUAD8	$-8.941\ 10^{-3}$	$-9.785\ 10^{-3}$	9.44
NASTRAN 64 QUAD8	$-8.972\ 10^{-3}$	$-9.929\ 10^{-3}$	10.67

transverse shear effects. Comparison is made with the three eight-node element meshes. The increase in the deflection of the plate is about ten percent in all three cases. Transverse shear, then cannot be neglected, especially when dealing with sandwich-based structure in which the core of the sandwich has much lower transverse shear stiffness than faces.

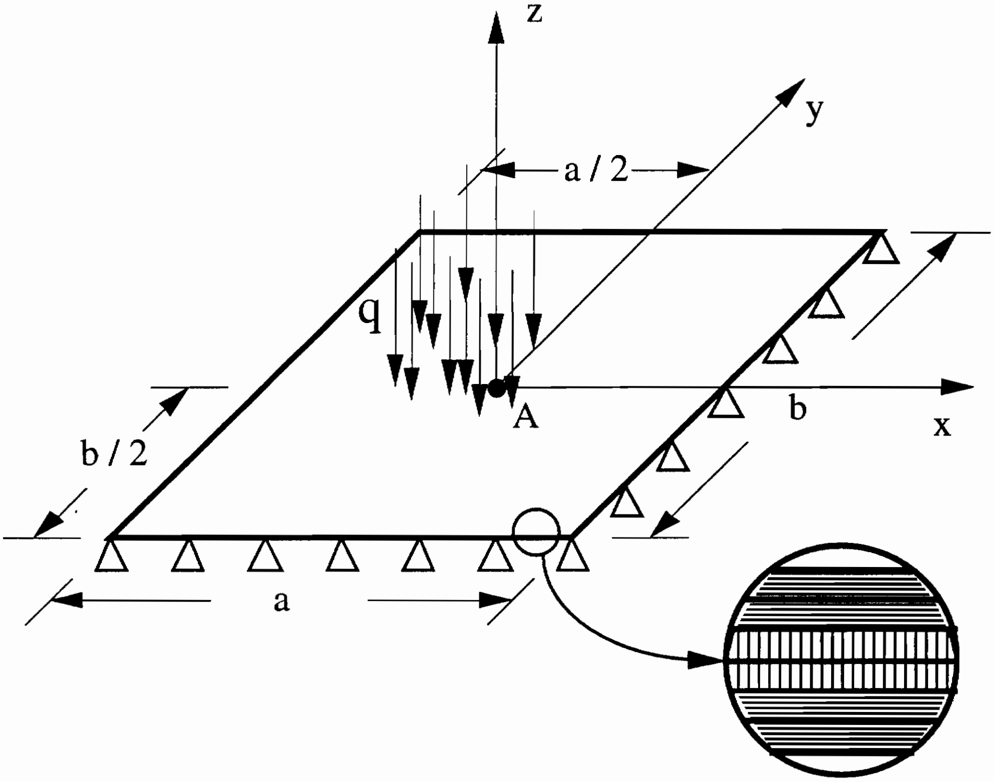

Figure 3.4 - Square simply supported laminated plate.

Next we considered a square simply supported composite plate with distributed load, to test the accuracy of the composite elements. The test plate is shown in Fig. 3.4. The plate measures a=b=8 mm, and is made of six layers of unidirectional graphite-epoxy Cycom 759, with a stacking sequence $[0°_2,90°]_s$, and a total thickness of 1.2 mm. The load $q=-10$ N/mm^2 is uniformly distributed on the plate. Material properties are:

$E_1=133.5\ 10^3$ MPa, $E_2=8.73\ 10^3$ MPa, $G_{12}=4.41\ 10^3$ MPa, and $\nu=0.304$.

The transverse displacement can be obtained analytically from classical lamination theory [10] as:

$$\text{(4.2)} \qquad w = \frac{16 q_o}{\pi^6} \sum_{m=1,2,..} \sum_{n=1,2,..} w_{mn} \sin\frac{m\pi x}{a} \sin\frac{n\pi y}{b}$$

where

$$\text{(4.3)} \qquad w_{mn} = \frac{1}{mn}\left[D_{11}\left(\frac{m}{a}\right)^4 + 2\left(D_{12}+2D_{66}\right)\left(\frac{m}{a}\right)^2\left(\frac{n}{b}\right)^2 + D_{22}\left(\frac{n}{b}\right)^4\right]^{-1}$$

and D_{11}, D_{12}, and D_{66} are the terms of the laminate bending stiffness matrix.

Two different approaches were used to model the laminate plate. The first approach was used with an old version of NASTRAN that did not have analysis capabilities for composite laminates. The laminate was then modeled using one plate element for each layer, and one to represent the laminate mid-surface. The plates were stacked up, and the corresponding nodes of each element were linked by a special rigid element to the ones on the mid-surface. This satisfied the hypothesis of Kirchhoff's plate theory. The basic cell, used as a superelement, was then reproduced to model the whole plate.

This approach was abandoned as the capability of easily inputting laminate stacking sequences became available, but it represented a useful test to evaluate accuracy of these rigid elements which were later used in the model. With this added capability the stacking sequence is given in a very simple fashion: for each ply, the thickness, the material, and the orientation of the material principal axes are inputted in an appropriate card. All plies are assembled according to the classical lamination theory [11], and a new card, containing properties for in-plane, bending and shear behavior for the plate elements, is generated and used in the analysis as property card for the plate elements.

As in the isotropic case, only a quarter-plate model was analyzed. For the first approach, the cells were composed of eight-node elements, and sixteen of these cells were used to mesh the quarter-plate model. In the second case, three different meshes were generated, all using eight-node elements.

Results obtained by these two approaches are shown in Table 3.3, and compared with those obtained using Eq. 4.2.

Table 3.3 - Center displacement for model of square simply supported laminated plate.

units = mm	W_A	error %
Eq. 4.2	$- 2.738\ 10^{-2}$	--
7 plies 16 cells QUAD8	$- 2.752\ 10^{-2}$	0.53
NASTRAN 4 QUAD8	$- 2.729\ 10^{-2}$	0.33
NASTRAN 16 QUAD8	$- 2.737\ 10^{-2}$	0.04
NASTRAN 64 QUAD8	$- 2.737\ 10^{-2}$	0.04

The seven-layer model, although quite precise in the results, is not really a viable way to model laminated plates. Besides its complexity, its geometry is very hard to change, since every single layer has to be modified. Even changing thickness of the plies requires the change of the coordinates of all plies. In contrast, he second model is very easy to use and gives good accuracy, even with low number of elements.

3.3 Modeling the carriage

We saw in Section 3.2, that for plates with aspect ratio similar to those of the panels of the carriage, we obtained acceptable results with only 4 elements per plate. However, this is only an indication of the obtainable accuracy and the situation in a more complex structure may be different. So, in modeling the carriage, one of the main tasks was to find a level of mesh refinement that gives acceptably accurate results at a low computational cost, needed for use in the optimization.

Various assumptions and simplifications were made in order to reduce the complexity of the structure. The symmetry of the structure was exploited and only half of the structure was modeled.

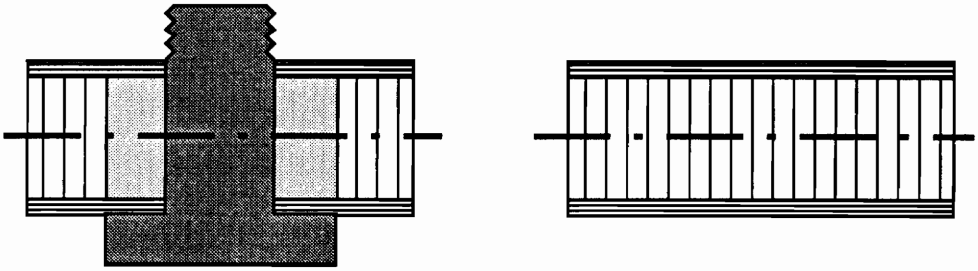

Figure 3.5 . - In the FE model, the inserts and the metal parts are not modeled.

One of the major assumptions was to analyze only the bare composite, Fig. 3.5, ignoring the metal parts used to connect the composite with other components of the machine, and the corresponding inserts embedded in the sandwich to provide local reinforcement for the panels. Most of these parts are small steel disks bolted on the panels, but others, as for example those providing support for the bearings, are quite large, and their dimensions are comparable with those of the sandwich panels. Being permanently attached to the composite they may influence the response of the structure.

As a first conservative approximation, however, we decided to neglect the contribution of the metal parts and the inserts. Plate elements were used to model the sandwich panels, although this approach may not be very accurate in some part of the structure as, for instance, near areas where the panels are attached to each other.

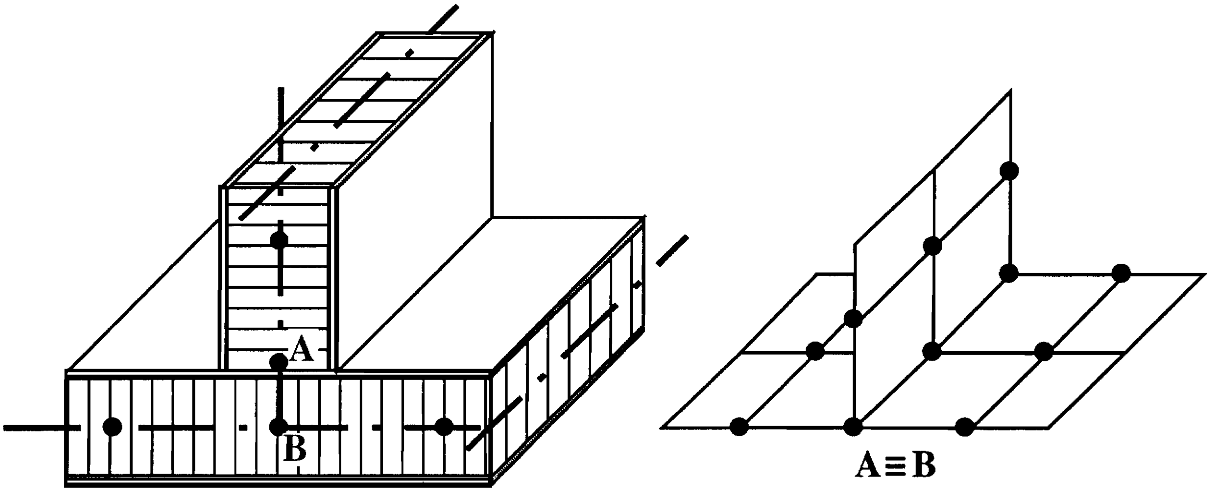

Figure 3.6 - Panel intersection, and its finite element model.

When two panels are joined together, as shown in Fig 3.6, bending moments are transferred from the skins of the top panel only to the top skin of the bottom panel, with the core of the top panel contributing little. Shear forces, instead, are transferred mostly by the core of the top panel, as the skins constitute a relatively small part of the surface of the cross section. The core of the bottom panel then transfers both loads from the top to the bottom skin. Failure of this type of joints is usually due to failure of the adhesive or delamination of the first plies of the top skin of the bottom panel. This local behavior is not modeled by the finite element model of the structure and may be a source of error in the results.

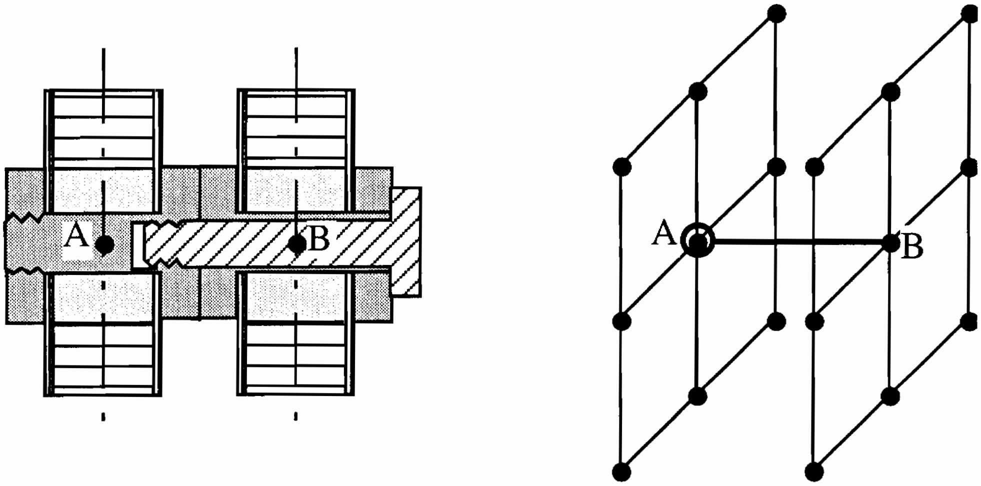

Figure 3.7 - Detail of joining between the interface and the support and the corresponding finite element model.

Rigid elements are used to model the two bolted joints that link the support to the interface, as shown in Fig. 3.7 by the rigid element AB. The bearings and their metal supports are initially not considered. The preload forces acting on the bearings are moved to points on the back panel of the interface, adding appropriate compensating moments, Fig. 3.8.

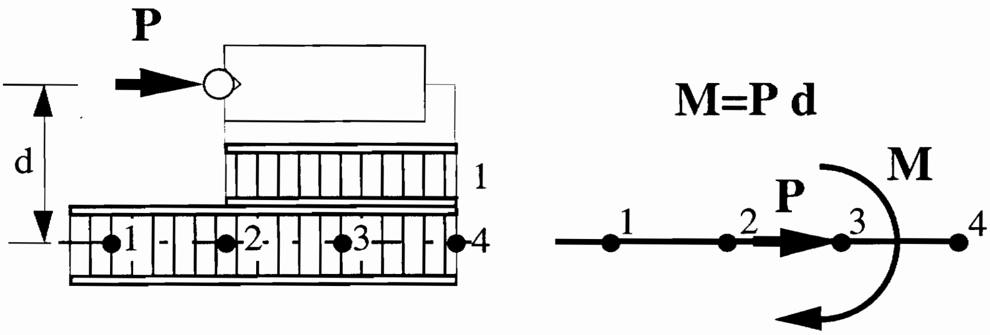

Figure 3.8 - Bearing preload forces and the corresponding finite element model.

As in the simple analysis that we presented before, the self weight of the structure was not considered. The assumption is acceptable if we consider that the total weight of the carriage is only about 50N, which is about one fourth of the load given by the sensor, and more than half of it, about 27N, is due to the metal bearing supports in the rear of the carriage. Of the set of loads acting in the front of the structure, Fig. 2.1, we only considered the weight of the sensor, modeled by two downward forces acting on the sensor attaching points[1]. As for the boundary conditions on the carriage, the Y displacement and the rotations about the X and the Z axes were constrained for all points lying in the plane of symmetry. The bearings constrain the displacement in the X direction and the rotation in the Y direction. Since the bearings were initially left out of the analysis, the boundary conditions were applied to the nodes on the back plate of the interface, where the preload forces act, Fig. 3.9.

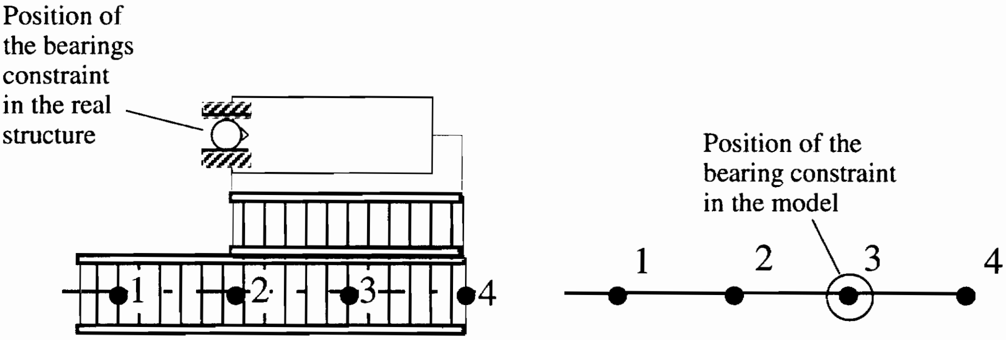

Figure 3.9 - Detail of the constraint due to the bearing.

The displacement in the Z direction was constrained in the points where

---

[1] There is no good reason for this assumption. The effects of the moments neglected here are however considered in section 4.8, on the integer number of plies design derived from the optimal design of optimization T45D20.

the linear actuators, or snails, are fixed to the interface. Recall that the carriage moves up and down along the machine, and the carriage, Z direction. The motion is given by a motor through a certain number of linear actuators, or snails, fixed on a thin metal plate, bolted on the back side of the carriage. In the equivalent static analysis we assumed that the snails act as a constraint for the carriage in the Z direction. This boundary condition is applied to the points where the plate carrying the snails is bolted to the carriage.

Running the plate examples we saw that even with a coarse mesh we could obtain accurate displacements, but the situation for a more complex structure may be different. We therefore created three different models for the carriage, having the same geometry but different level of refinement :

1 - a first model, based on a very coarse mesh of four-node elements, shown in Fig. 3.10;
2 - an intermediate model, sharing the same mesh of the first one but using eight-node elements in place of four-node, shown in Fig. 3.11.
3 - a finer model, having a finer mesh than the first two and using eight-node elements, shown in Fig. 3.12.

The displacements of five points of the structure were compared: the three points where the snails are fixed to the structure, on the rear panel of the interface, and the two points where the sensor is attached to the support, in the front of the carriage. We recall that the X displacement of the first three points, and the Z displacement of the second two was required by Speroni to be less than about 10 and 4 microns, respectively. This set of five displacements will be referred to as the basic set of

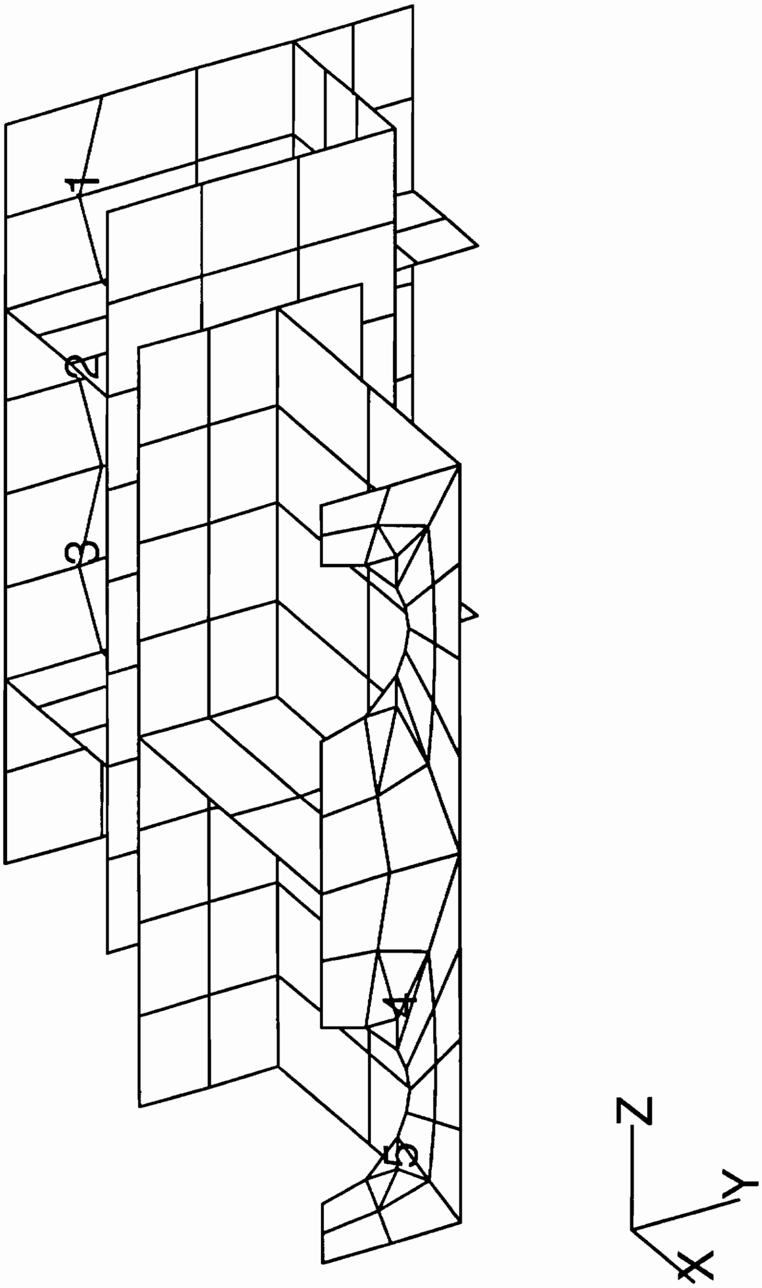

Figure 3.10 - First model: coarse mesh and four-node elements

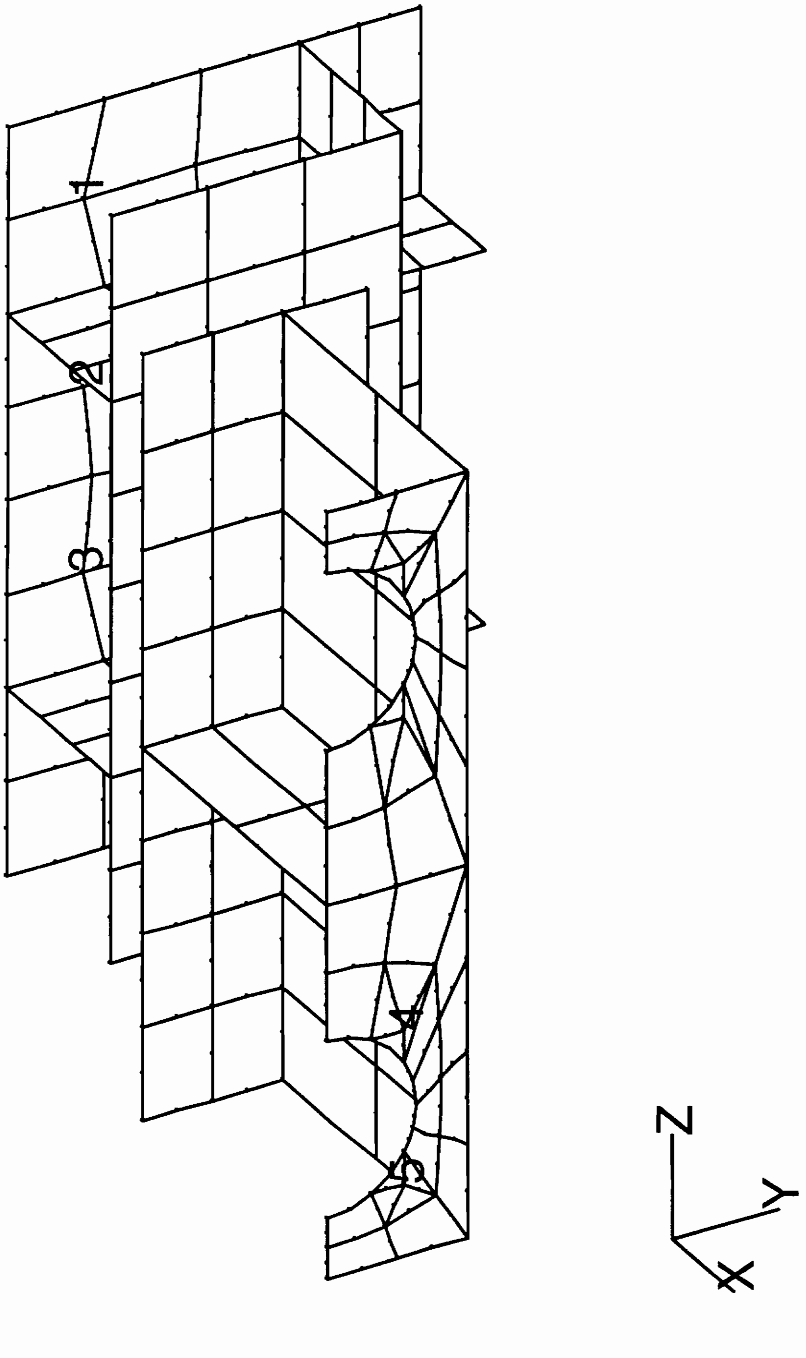

Figure 3.11 - Intermediate model: coarse mesh and eight-node elements

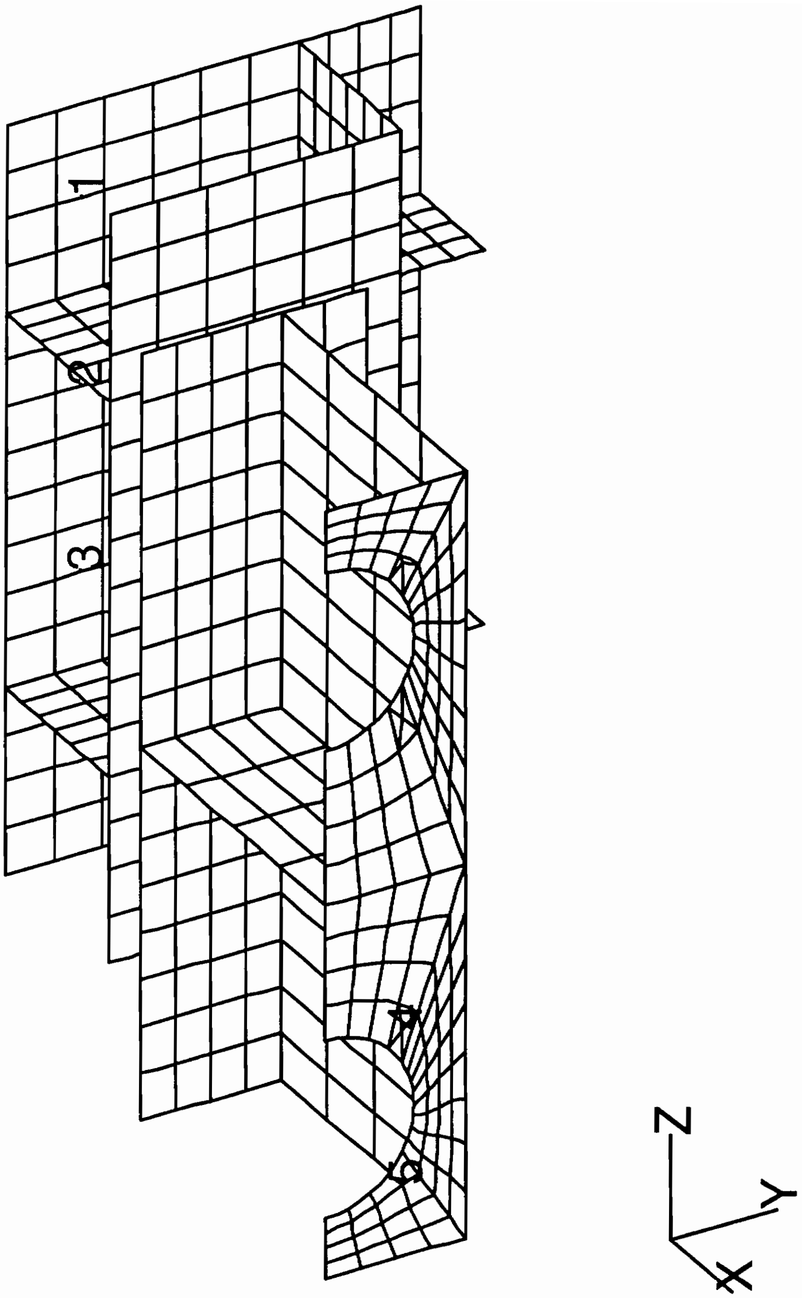

Figure 3.12 - Finer model: finer mesh and eight-node elements

displacements, while the set of points they belong to, will be called the basic set of points. In the finite element analysis, and even more in the optimization, we will also consider an extended set of points, that includes the basic set, and the four connecting points where the two substructures are connected to each other. This will allow us to separate the contribution of the two substructures and determine which one has to be redesigned.

An all aluminum carriage, having the same dimensions and panel thicknesses of the composite carriage, was analyzed first to test the meshes. The displacements of the basic set were compared to check the convergence of the solution. The mass of the models was also calculated and compared with the nominal one.

Table 3.4 - Results of the three model using aluminum.

Units = micron Node & component	First Model	Intermediate model	Finer model	Calculated with a strength-of-materials approach.
node 1 along x	-1.156	-1.165(0.74)	-1.168(.28)	0.789
node 2 along x	-1.329	-1.357(2.15)	-1.397(3.03)	
node 3 along x	-1.906	-1.878(-1.45)	-1.930(.2)	
node 4 along z	-3.428	-3.988(16.34)	-4.381(11.45)	0.075
node 5 along z	-3.600	-4.199(16.64)	-4.539(9.46)	
mass	223.4	223.3	223.3	225.0
Nodes 1, 2 and 3 are the snail nodes, top, medium, and bottom. Nodes 4 and 5 are the sensor nodes.				

Table 3.4 shows the results obtained with the different models. The numbers in parenthesis in column three and four are the percent difference with the corresponding coarser mesh. Results seem to converge from the first model to the finer, for almost all five displacements. The masses of the three models are quite the same and agree well with the actual mass. The

displacements were also calculated in a way similar to that shown in sec 2.4 for the composite carriage. The calculated displacement for the snail points is actually that of the mid span of the back plate of the interface, which is very close to the attachments for the snail plate, points 1, 2, and 3. Considering the approximations used to calculated it, the displacement at the snail points agreed quite well with those obtained through finite element analysis, while at the sensor the displacements were greatly underestimated.

The composite carriages were analyzed next. The mechanical properties of the materials used in the analysis of the composite carriage, are shown in Table 2.1. As mentioned earlier, for the skins we used unidirectional and fabric graphite-epoxy prepregs, while for the core we used Nomex paper honeycomb. Table 3.5 shows the basic set of displacements for the three models. The number of nodes, elements, and the CPU time are also given.

For the intermediate and the finer model we show in parenthesis the percent difference with respect to the corresponding coarser mesh. Computational time is given in terms of both CPU time and User time, i.e. the actual time elapsed between the beginning and the end of the analysis. For all displacements we can see a convergence in the values, going from the first to the finer model. On the average the difference in the magnitude of the displacements was 24.93 percent going from the first to the intermediate model, and 6.61 percent going from the latter to the finer model. As for the aluminum carriage, the displacements calculated with the strength of materials approach were of the right order of magnitude at the snail points, within the limits of the approximation of the method, but too small at the sensor points. One of the possible explanations is that the simple beam model used to calculate the displacement at the snail points, is close enough to the real behavior of the interface, and the two cantilevered beams model used to calculate the transverse displacement of the carriage are instead totally inaccurate.

Table 3.5 - Comparison of the results of the three models for the composite carriage.

Units = micron	First model: coarse mesh QUAD4 El.	Intermediate model: coarse mesh QUAD8 El.	Finer model: finer mesh QUAD8 El.	Calculated in Section 2.4
nodes	234	681	2441	-
elements	215	215	769	-
node 1 along x	-9.5	-6.1 (36.06)	-4.5 (24.6)	6.8
node 2 along x	-16.9	-18.1 (6.31)	-18.39 (1.94)	
node 3 along x	-27.84	-30.3 (8.91)	-31.6 (4.12)	
node 4 along z	-302.0	-463.3 (53.41)	-497.4 (7.36)	2.0
node 5 along z	-304.2	-466.0 (21.43)	-495.4 (6.31)	
User time (min:sec)	0:15.2	1:10.0	3:32.0	-
CPU time (min:sec)	0:08.2	0:14.6	0:31.5	-
Nodes 1, 2 and 3 are the snail nodes, top, medium, and bottom. Nodes 4 and 5 are the sensor nodes.				

The CPU time almost doubled going from the first model to the intermediate model, and doubled again going to the finer model. One could expect a larger increase in the CPU time, considering that the finer model almost quadruples the number of nodes of the intermediate. The reason probably lies in the sparse solver used in the analysis, whose performance improves with the dimension and the relative sparsness of the matrix. If we look at the user time, however, we notice that it almost triples from the intermediate model to the finer model, increasing from about one minute to about three minutes. Thinking in terms of optimization, if we needed 120 analyses, the run time would be two hours for the intermediate model, and six for the finer model. Furthermore several optimization runs may be needed.

Because of the computational cost, and since we are more interested in comparing different designs rather than in calculating displacements with high accuracy, we decided that the intermediate model was a good compromise between sufficient accuracy and affordable computer time. The first model, however, was still used to investigate the effects of small variations in the modeling assumptions, requiring geometric changes, which were easier to make on a smaller model.

3.4 New modeling assumptions

The behavior of the structure under thermal loads was one of the major concerns of this work, and metal parts are much more affected by temperature changes than composites, thus representing a big source of thermal deformations. In order to accommodate the bearings and their supports, the model was slightly changed. The basic set of displacements was checked step by step during these changes.

1 - First the preload forces were moved from the back plate of the interface to their actual position by adding new points and connecting them to facing points on the interface through rigid elements.

2 - The bearings supports were then added to the model as metal layers in the stacking sequence of the corresponding elements of the interface.

3 - Boundary conditions due to bearings were applied to the new points to which preload forces were moved.

Results of these changes are displayed in Table 3.6. Moving the preload forces did not affect the considered displacements at all. Introducing the bearings and their supports produced the results of stiffening the interface for bending about the Y axes. This can be seen from the fact that the X displacement of nodes 1 to 3 are now closer to each other than they were before. Finally, moving the constraints to their real positions, helped the interface for bending about the Z axes, reducing the displacements of the first three points.

Table 3.6 - Changes in displacements due to new model assumptions.

Units = micron	first model Table 3.4	change #1	change #2	change #3
⇨ Preload force ● Constrained node ··· Rigid element	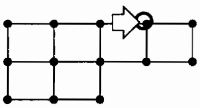	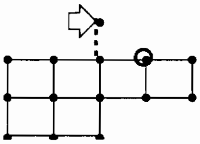	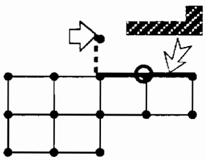	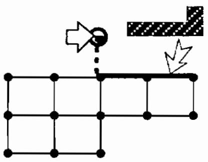
node 1 along x	-9.5	-9.3	-11.7	-15.3
node 2 along x	-16.9	-16.6	-22.0	-18.9
node 3 along x	-27.84	-27.5	-29.9	-20.9
node 4 along z	-302.0	-302.2	-290.6	-275.4
node 5 along z	-304.2	-304.2	-292.7	-277.6
Nodes 1, 2 and 3 are the snail nodes, top, medium, and bottom. Nodes 4 and 5 are the sensor nodes.				

The displacements of the sensor points changed very little during all these changes. However it was noticed that results were sensitive to the position of the rigid elements linking the points where preload forces are now applied to the back plate of the interface. We then decided to separate the contribution of the metal bearing supports from the back plate of the interface and model them with separate new elements. Displacements after a change in the position of the rigid elements and results for the new model are presented in Table 3.7. The last column of the table shows how transverse shear deformation of the honeycomb affects the value of the displacements. The model is the same as in the previous column but with infinite transverse shear modulus for the core.

Table 3.7 - Changes in displacements due to new model assumptions.

Units = micron	change #3	change #4	new model	no shear
⇨ Preload force ◉ Constrained node ··· Rigid element	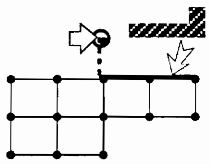	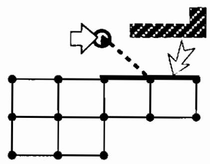	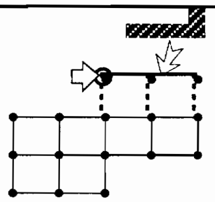	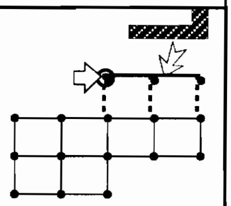
node 1 along x	-15.3	-52.9	-9.8	-7.3
node 2 along x	-18.9	-7.3	-13.1	-6.2
node 3 along x	-20.9	-14.6	-14.7	-7.2
node 4 along z	-275.4	-292.3	-274.3	-32.5
node 5 along z	-277.6	-294.5	-276.5	-40.0
Nodes 1, 2 and 3 are the snail nodes, top, medium, and bottom. Nodes 4 and 5 are the sensor nodes.				

Next we added thermal properties of the materials, Table 3.8, and we loaded the structure with thermal loads. Thermal expansion coefficients for the composites have been taken from [6], and correspond to materials similar to those used in the analysis. The performance of the machine is guaranteed by the manufacturers, in a temperature range of 5°C to 45°C. As thermal load we considered a uniform increase from a reasonable average temperature of 20°C to 15°C above the maximum allowable temperature, i.e. to 60°C. Since the temperature change was one of the main sources of deformation for the structure, designing with a higher final temperature would have given us conservative solutions.

Table 3.8 - Thermal expansion coefficients.

Units = mm / mm °C	α_x	α_x
UD	0.02 10^{-6}	22.5 10^{-6}
Fabric	0.10 10^{-6}	0.10 10^{-6}
Steel	13.0 10^{-6}	

To separate the contribution of the two different materials, the thermal load was applied first to the composite only, then to the bearings and the metallic support only, and finally to both the bearings and the composite. Results are given in Table 3.9. Application of the thermal load to the structure led to very little changes in the values of the displacements of the basic set. Average change for the snail points, 1, 2, and 3, was about 4 percent, while that of the sensor points, 4 and 5, was around 5 percent. What is more important is that, if we consider the three snail points, for instance, the difference between their displacements was reduced by the application of the thermal load. If we consider the position of the three points in one of the figures showing the models, Fig, 3.10 to Fig. 3.12, we can see that a difference in their displacements means a bending of the back plate of the interface about the Y axes, or a non vertical position of the plate. The larger the difference, the higher the bending deformation of the plate, and consequently a higher bending of the motor shaft. Since bending of the motor shaft is an unwanted effect, we should then conclude that the thermal load had a good effect on the behavior of the structure. At least, within the approximation of the finite element analysis, and within the displacements of the basic set.

Table 3.9 - Application of thermal load to the carriage.

Units = microns Node & component	New model in Table 3.7	Composite only	Bearing supports only	Both
node 1 along x	-9.8	-7.8 (-21.0)	-12.1 (23.5)	-10.1 (2.6)
node 2 along x	-13.1	-11.5 (-12.1)	-13.8 (5.7)	-12.3 (-6.4)
node 3 along x	-14.7	-13.1 (-11.2)	-15.5 (4.9)	-13.8 (-6.3)
node 4 along z	-274.3	-288.7 (5.2)	-271.2 (-1.2)	-285.5 (4.1)
node 5 along z	-276.5	-296.5 (7.3)	-273.3 (-1.2)	-293.3 (6.1)
1(X) - 2(X)	-3.3	-3.7 (14.6)	-1.7 (-48.0)	-2.2 (-33.3)
1(X) - 3(X)	-4.9	-5.3 (8.2)	-3.3 (-32.2)	-3.7 (-24.0)
4(Z) - 5(Z)	-112.2	-111.8 (-0.3)	-110.4 (-1.6)	-110.0 (-1.9)

Nodes 1, 2 and 3 are the snail nodes, top, medium, and bottom. Nodes 4 and 5 are the sensor nodes.

The effects on a larger structure, such as, for instance the tower, may be very different. Also, the results of the application of the load to only one of the materials, resulted in an increase of the displacements when applied to the bearings only, and in an increase of the value of the differences when applied to the composite only. This suggest that different thermal loads and different gradients of temperature may be considered to better evaluate the behavior of the structure.

4 Sensitivity Analysis and Optimization

4.1 Introduction

In the previous chapters we gave some background on coordinate measurement machines, with more details about Speroni models. We saw that Speroni is trying to improve substantially the performance of their machines by replacing their heavy steel structures with much lighter composite ones, and how they had started this process, building a tower and a carriage for one of their machines.

We saw how we moved a step forward by considering the redesign of the carriage of the machine, which is the smallest element of the structure, but a very important one. We described how we designed, and built a prototype of the carriage, made with Nomex core and graphite-epoxy laminate skin sandwich panels, considerably reducing its weight from 100 to about 15 kilograms. Finally we saw the finite element model of the prototypal carriage that we built in order to analyze it and to perform structural optimization.

4.2 The Optimization Problem

The design, analysis, and optimization of the composite carriage was intended to be a trial project, a small problem that could increase our experience in both the design and the manufacturing of composite materials. This increased experience could help us in the design of the other larger components of the structure of the machine.

One of the key issues of the project was how to reduce the effects of temperature changes, that, particularly on the large components, caused unpredictable deformations, reducing the precision and the repeatability of the measurements. The object of the design was then to reconfigure the stacking sequence and the thicknesses of the panels to reduce thermal deformations. For the carriage, however, the temperature load seemed to have smaller influence than expected on the deformations of the structure, as shown by Table 3.9. In the basic set of displacements, the maximum difference between the structure with and without the thermal loading, was 6.4 percent, and the average difference was only 5.1 percent. For this reason we decided to consider the displacements as constrained responses rather than an objective function to minimize, and optimize the structure for minimum weight, W. The design variables of the optimization problem will be the thicknesses of each ply of the skins, and the thickness of the core of each panel.

The optimization problem can thus be stated as

$$\min_{t_{ij}} \quad W \tag{4.1}$$

$$\text{S.T.} \quad |u_l| < c_l \qquad l = 1,..,N_r \tag{4.2}$$

$$t_{ij}^L < t_{ij} < t_{ij}^U \qquad i,j = 1,..,N_d \tag{4.3}$$

where u_l is the l^{th} displacement of the basic set of points, Fig. 4.1, and c_l is the maximum allowable value for the l^{th} displacement, t_{ij} is the thickness of the i^{th} ply of the j^{th} panel and $t^L{}_{ij}$ and $t^U{}_{ij}$ are respectively the upper and the lower bound for the thickness of the ij^{th} ply. N_r and N_d are the number of constrained displacement components and design variables, respectively.

The values of the displacement limits are set to 4 microns for the snail points, 14, 64 and 86, and 10 microns for the sensor points, 2003 and 2004.

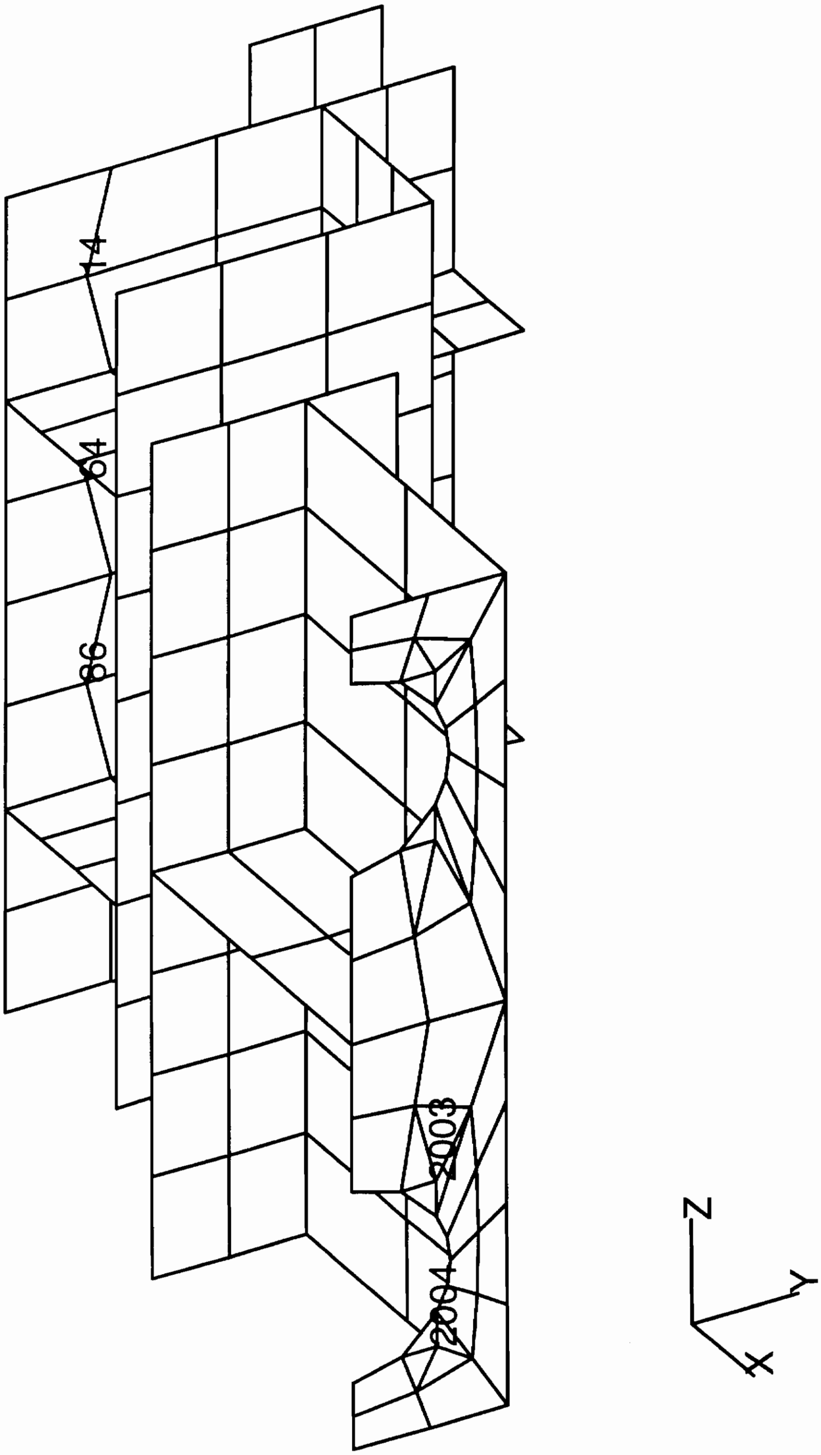

Figure 4.1 - Basic set of points used in the sensitivity analysis

4.3 Structural Optimization in MSC/NASTRAN

The optimization routine implemented in MSC/NASTRAN [12], uses a gradient based method for the search of the optimum design. More precisely, the Modified Method of Feasible Directions [13], is implemented. The method identifies at each step a "usable-feasible" direction, i.e. a direction that reduces the value of the objective function (usable), but also does not violate the constraints (feasible). The search direction is evaluated in different ways: if none of the constraints is violated, the direction of the steepest descent is used to start the search, that is continued along conjugate directions. If one or more constraints are violated, or nearly violated, a suboptimization problem is solved to find a search direction that points back into the feasible region, in case the design is infeasible, or a direction that points away from the near violated constraints. Once the search direction is found, a one-dimensional search is performed to find the optimal step size to be taken in the search direction.

The constraints of the problem are normalized with respect to the corresponding limit values, and transformed to the form $g(x) \leq 0$. A threshold is used to screen the constraints to identify the active ones, and among all active only the N most violated or closest to be violated are used to guide the search. The threshold value as well as the maximum number of considered constraints N can be selected by the user.

The design responses are approximated using simple Taylor expansion series, function of the design variables or of their reciprocals, depending on the kind of design response (convex linearization is also available, but its use is suggested only as a "research capability"). The optimization is carried out with the approximated constraints. Because of the approximation, critical constraints may be found, on analysis of the optimal design, to have small positive or negative constraint margins.

4.4 Design Model

The design model for the optimization is based on the intermediate of the three models that were described in Section 3.3, modified to incorporate the new assumptions described in Section 3.4.

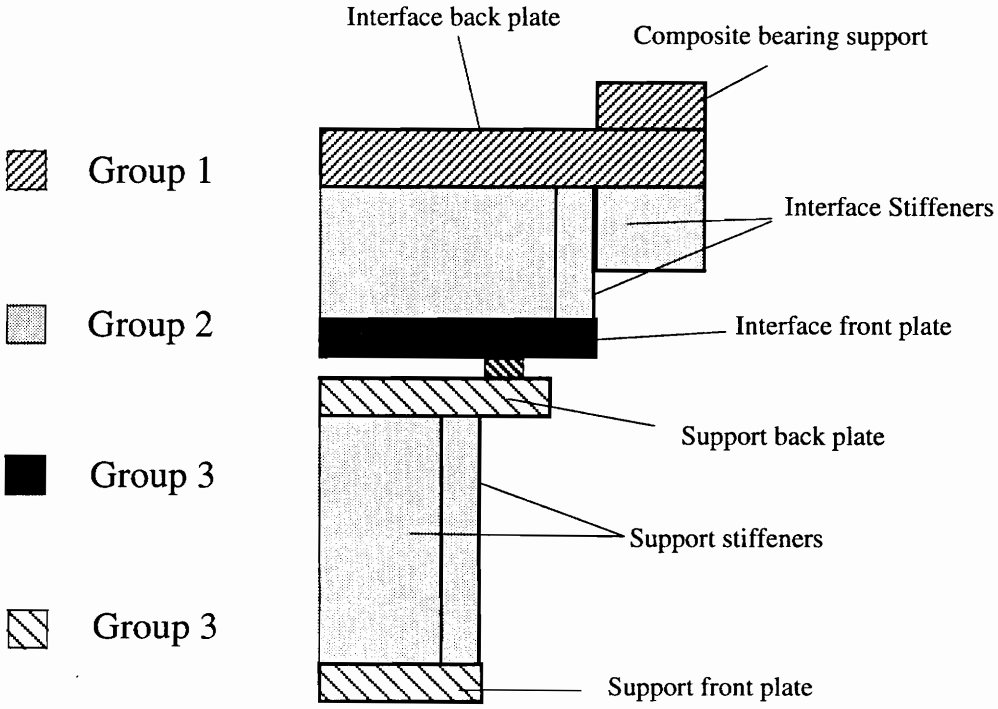

Figure 4.2 - Grouping of the panels of the carriage.

The structure of the carriage is made of eight sandwich panels, with two, the horizontal stiffeners in the interface, being identical and thus described by the same property card in the finite element model. Due to the symmetry of the panels and the symmetry of the laminate skins, each panel can be described with only three design variables, two for the skins and one for the core, adding up a total of 21 design variables in the whole structure. Keeping all 21 variables, however, would probably result in a design having seven different laminate lay-ups, and different honeycomb core thickness.

To reduce the number of different panels, in order to make manufacturing easier and reduce costs, the panels are initially grouped into four groups:

group 1 - back plate of the interface;
group 2 - all stiffeners of both the interface and the support;
group 3 - front plate of the interface;
group 4 - back and front plates of the support.

The grouping reduced the number of independent variables to 12, denoted as T_i, i=1,..,12 , regardless of what panel they belong to. Figure 4.2 shows the different groups, while Fig. 4.3 shows their corresponding lay-ups and design variables.

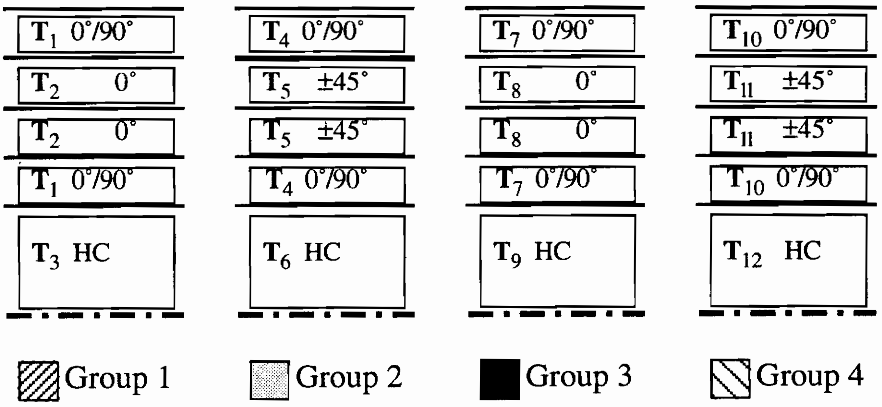

Figure 4.3 - Panel lay-ups and design variables.

4.5 Sensitivity Analysis

The starting design for the optimization is given by the actual thicknesses of the prototypal carriage. To simplify the search for optimum designs the constraint on the displacement of the sensor points was relaxed, increasing the maximum allowable value from 4 microns to 10 microns, which is equal to the value of the limit at the other three points.

A sensitivity analysis of the structure was performed. The sensitivities of the objective function *W*, and the five design responses u_j, with respect to the twelve design variables, are given in Table 4.1.

Table 4.1 - Matrix of sensitivity coefficients, $\frac{\partial W}{\partial T_i}$, and $\frac{\partial u_j}{\partial T_i}$, j=1,...,5.

Variable	Weight	u_1 Node 14 along X	u_2 Node 64 along X	u_3 Node 86 along X	u_4 Node 2003 along Z	u_5 Node 2004 along Z
Units	(N/mm)	(mm/mm)	(mm/mm)	(mm/mm)	(mm/mm)	(mm/mm)
T_1	5.691800	-0.002052	0.007968	0.007563	0.032898	0.032898
T_2	5.442000	0.045429	0.028539	0.029711	0.015378	0.015354
T_3	0.049807	0.000836	0.000379	0.000514	0.000864	0.000864
T_4	10.200000	0.018847	0.008518	0.009805	0.032658	0.033811
T_5	10.200000	0.006491	0.000839	0.005256	0.047001	0.047934
T_6	0.168430	0.000295	-0.000077	-0.000088	0.002655	0.002658
T_7	4.366800	0.006040	0.003441	0.005052	0.204280	0.204310
T_8	4.172800	-0.004262	-0.004224	-0.002737	0.104860	0.105290
T_9	0.045347	-0.000025	0.000045	0.000050	0.021496	0.021500
T_{10}	5.158400	0.000426	0.000062	0.000252	0.052087	0.056211
T_{11}	5.158400	0.000400	-0.000001	0.000223	0.054404	0.056903
T_{12}	0.039730	-0.000003	0.000012	0.000013	0.014080	0.014112

Examining the sensitivities, one could conclude that the cores of the panels, described by the variables T_3, T_6, T_9, and T_{12} play a marginal role compared to the plies of the skins, since their sensitivities are much smaller than those of the laminates. However, these dimensional derivatives can be misleading because variables with large magnitudes tend to have smaller sensitivities than variables with small magnitude. For example a 1 mm increase in the thickness of one of the plies in the skin of the sandwich triples its thickness, while the same variation in the thickness of the core represents only a 3 to 5 percent increase.

A better measure of the magnitude of the sensitivities can be obtained by considering the nondimensional logarithmic sensitivities of the displacements, defined as

$$\frac{\partial_\ell u_j}{\partial_\ell T_i} = \frac{\partial u_j}{\partial T_i}\frac{T_i}{u_i} \tag{4.4}$$

This derivative is roughly the percent increase in the displacement component due to a 1 percent increase in the design variable. Another good measure to consider when comparing design variables is the weight effectiveness, defined as the ratio between the change in displacement derivative and the corresponding weight derivative

$$\left(\frac{\partial u_j}{\partial W}\right)_i = \frac{\dfrac{\partial u_j}{\partial T_i}}{\dfrac{\partial W}{\partial T_i}} \tag{4.5}$$

Again we can consider the logarithmic version of the derivative given by eq. 4.5 and obtain:

$$\left(\frac{\partial_\ell u_j}{\partial_\ell W}\right)_i = \left(\frac{\partial u_j}{\partial W}\right)_i \frac{W_i}{u_j} \tag{4.6}$$

The weight effectiveness represents the expected change in displacement for a given change in the weight of the structure. In other words, if we are willing to pay a one percent increase in weight to reduce the value of the displacement, the largest negative weight effectiveness in the form shown by eq. 4.6, tells us which design variables will give us the largest decrease.

The last parameter that we want to consider is the percent of the total weight of the structure corresponding to each design variable that tells us the influence of each variable on the weight of the structure.

$$(4.7) \qquad w_i = \frac{W_i}{W} = \frac{\frac{\partial W}{\partial T_i} T_i}{W}$$

From eq. 4.4 we can derive the percent change in one of the displacements in terms of the percent change in one of the thicknesses p_i.

$$(4.7) \qquad \frac{\Delta u_j}{u_j} = \frac{\partial_\ell u_j}{\partial_\ell T_i} \frac{\Delta T_i}{T_i} = \frac{\partial_\ell u_j}{\partial_\ell T_i} \frac{p_i}{100}$$

Doubling one of the thicknesses, corresponds to a value of p_i 100, and the logarithmic sensitivity of the displacement given by eq. 4.4 represents the hypothetical change in the displacement. This change is, however, approximate, since it is based on a linear approximation. Table 4.2 gives the initial value of the design variables T_i and the design responses W and u_j. These values are used to calculate the effectiveness and logarithmic sensitivities shown in Tables 4.3 to 4.7.

Tables 4.3 to 4.5, present the logarithmic sensitivities and weight effectiveness for the displacement of the snail points. The values of the displacement sensitivities are very small, indicating that even a substantial change in some of the thicknesses would produce a much smaller change in the displacements. The core and the unidirectional plies in the skins of the back panel of the interface, T_2 and T_3 respectively, are the driving variables, while all other variables have much smaller or almost no influence.

Table 4.2 - Initial value of the design variables and the design responses

T_1 =0.310	T_2 =0.125	T_3 =14.30	T_4 =0.310	T_5 =0.310	T_6 =0.950
T_7 =0.310	T_8 =0.125	T_9 =0.950	T_{10} =0.310	T_{11} =0.310	T_{12} =0.950
Weight	u_1	u_2	u_3	u_4	u_5
45.032	-10.5	-13.9	-15.8	-391.1	-399.5
Units: thicknesses in mm, displacements in micron and weight in N					

Table 4.3 - Logarithmic sensitivities and weight effectiveness for displacement u_1, node 14 (snail top) along X.

Variable	$\frac{W_i}{W}$	$\frac{\partial u_j}{\partial T_i}$	$\frac{\partial u_j}{\partial W_i}$	$\frac{\partial_\ell u_j}{\partial_\ell T_i}$	$\frac{\partial_\ell u_j}{\partial_\ell W_i}$
Units	-	mm/mm	mm/N	-	-
T_1	0.039182	-0.002052	-0.000361	0.060724	1.549789
T_2	0.015106	0.045429	0.008348	-0.542031	-35.882046
T_3	0.015816	0.000836	0.016791	-1.141509	-72.172913
T_4	0.070217	0.018847	0.001848	-0.557680	-7.942269
T_5	0.070217	0.006491	0.000636	-0.192077	-2.735483
T_6	0.035532	0.000295	0.001752	-0.267574	-7.530484
T_7	0.030061	0.006040	0.001383	-0.178726	-5.945431
T_8	0.011583	-0.004262	-0.001021	0.050858	4.390757
T_9	0.009566	-0.000025	-0.000562	0.023095	2.414159
T_{10}	0.035510	0.000426	0.000083	-0.012596	-0.354724
T_{11}	0.035510	0.000400	0.000078	-0.011832	-0.333201
T_{12}	0.008381	-0.000003	-0.000085	0.003049	0.363797

Table 4.4 - Logarithmic sensitivities and weight effectiveness for displacement u_2, node 64 (snail middle) along X.

Variable	$\frac{W_i}{W}$	$\frac{\partial u_j}{\partial T_i}$	$\frac{\partial u_j}{\partial W_i}$	$\frac{\partial_\ell u_j}{\partial_\ell T_i}$	$\frac{\partial_\ell u_j}{\partial_\ell W_i}$
Units	-	mm/mm	mm/N	-	-
T_1	0.039182	0.007968	0.001400	-0.178078	-4.544866
T_2	0.015106	0.028539	0.005244	-0.257200	-17.026424
T_3	0.015816	0.000379	0.007606	-0.390573	-24.694328
T_4	0.070217	0.008518	0.000835	-0.190380	-2.711320
T_5	0.070217	0.000839	0.000082	-0.018747	-0.266991
T_6	0.035532	-0.000077	-0.000459	0.052918	1.489306
T_7	0.030061	0.003441	0.000788	-0.076910	-2.558452
T_8	0.011583	-0.004224	-0.001012	0.038065	3.286311
T_9	0.009566	0.000045	0.001002	-0.031109	-3.251863
T_{10}	0.035510	0.000062	0.000012	-0.001397	-0.039331
T_{11}	0.035510	-0.000001	0.000000	0.000027	0.000756
T_{12}	0.008381	0.000012	0.000307	-0.008366	-0.998201

Table 4.5 - Logarithmic sensitivities and weight effectiveness for displacement u_3, node 86 (snail bottom) along X.

Variable	$\frac{W_i}{W}$	$\frac{\partial u_j}{\partial T_i}$	$\frac{\partial u_j}{\partial W_i}$	$\frac{\partial_\ell u_j}{\partial_\ell T_i}$	$\frac{\partial_\ell u_j}{\partial_\ell W_i}$
Units	-	mm/mm	mm/N	-	-
T_1	0.039182	0.007563	0.001329	-0.148477	-3.789395
T_2	0.015106	0.029711	0.005460	-0.235200	-15.570046
T_3	0.015816	0.000514	0.010312	-0.465135	-29.408594
T_4	0.070217	0.009805	0.000961	-0.192489	-2.741355
T_5	0.070217	0.005256	0.000515	-0.103193	-1.469641
T_6	0.035532	-0.000088	-0.000520	0.052646	1.481646
T_7	0.030061	0.005052	0.001157	-0.099182	-3.299371
T_8	0.011583	-0.002737	-0.000656	0.021669	1.870794
T_9	0.009566	0.000050	0.001094	-0.029856	-3.120923
T_{10}	0.035510	0.000252	0.000049	-0.004943	-0.139188
T_{11}	0.035510	0.000223	0.000043	-0.004376	-0.123244
T_{12}	0.008381	0.000013	0.000330	-0.007892	-0.941558

Table 4.6 - Logarithmic sensitivities and weight effectiveness for displacement u_4, node 2003 (sensor top) along Z.

Variable	$\frac{W_i}{W}$	$\frac{\partial u_j}{\partial T_i}$	$\frac{\partial u_j}{\partial W_i}$	$\frac{\partial_\ell u_j}{\partial_\ell T_i}$	$\frac{\partial_\ell u_j}{\partial_\ell W_i}$
Units	-	mm/mm	mm/N	-	-
T_1	0.039182	0.032898	0.005780	-0.025527	-0.651505
T_2	0.015106	0.015378	0.002826	-0.004812	-0.318522
T_3	0.015816	0.000864	0.017352	-0.030936	-1.955946
T_4	0.070217	0.032658	0.003202	-0.025341	-0.360900
T_5	0.070217	0.047001	0.004608	-0.036471	-0.519403
T_6	0.035532	0.002655	0.015764	-0.063139	-1.776951
T_7	0.030061	0.204280	0.046780	-0.158513	-5.273030
T_8	0.011583	0.104860	0.025129	-0.032809	-2.832566
T_9	0.009566	0.021496	0.474034	-0.511161	-53.432659
T_{10}	0.035510	0.052087	0.010098	-0.040417	-1.138183
T_{11}	0.035510	0.054404	0.010547	-0.042215	-1.188813
T_{12}	0.008381	0.014080	0.354392	-0.334813	-39.946781

Table 4.7 - Logarithmic sensitivities and weight effectiveness for displacement u_5, node 2004 (sensor bottom) along Z.

Variable	$\frac{W_i}{W}$	$\frac{\partial u_j}{\partial T_i}$	$\frac{\partial u_j}{\partial W_i}$	$\frac{\partial_\ell u_j}{\partial_\ell T_i}$	$\frac{\partial_\ell u_j}{\partial_\ell W_i}$
Units	-	mm/mm	mm/N	-	-
T_1	0.039182	0.032898	0.005780	-0.026073	-0.665437
T_2	0.015106	0.015354	0.002821	-0.004907	-0.324825
T_3	0.015816	0.000864	0.017352	-0.031597	-1.997772
T_4	0.070217	0.033811	0.003315	-0.026797	-0.381632
T_5	0.070217	0.047934	0.004699	-0.037990	-0.541041
T_6	0.035532	0.002658	0.015782	-0.064560	-1.816933
T_7	0.030061	0.204310	0.046787	-0.161926	-5.386582
T_8	0.011583	0.105290	0.025232	-0.033648	-2.905002
T_9	0.009566	0.021500	0.474122	-0.522189	-54.585442
T_{10}	0.035510	0.056211	0.010897	-0.044550	-1.254565
T_{11}	0.035510	0.056903	0.011031	-0.045099	-1.270010
T_{12}	0.008381	0.014112	0.355198	-0.342750	-40.893749

The last two tables present the sensitivities for the displacements of the sensor points. The largest values correspond to the variables that define the thickness of the core of the front and back plate of the support, T_{12}, and that of the front plate of the interface, T_9, followed by the variable defining the unidirectional plies of the skin of the latter panel, T_8. Surprisingly the variables related to the stiffeners of the support, T_4 through T_6, have very little influence on the value of the displacements of the sensor points. This may indicate that the deformation of the support is mainly due to the deformation of its front and back plates.

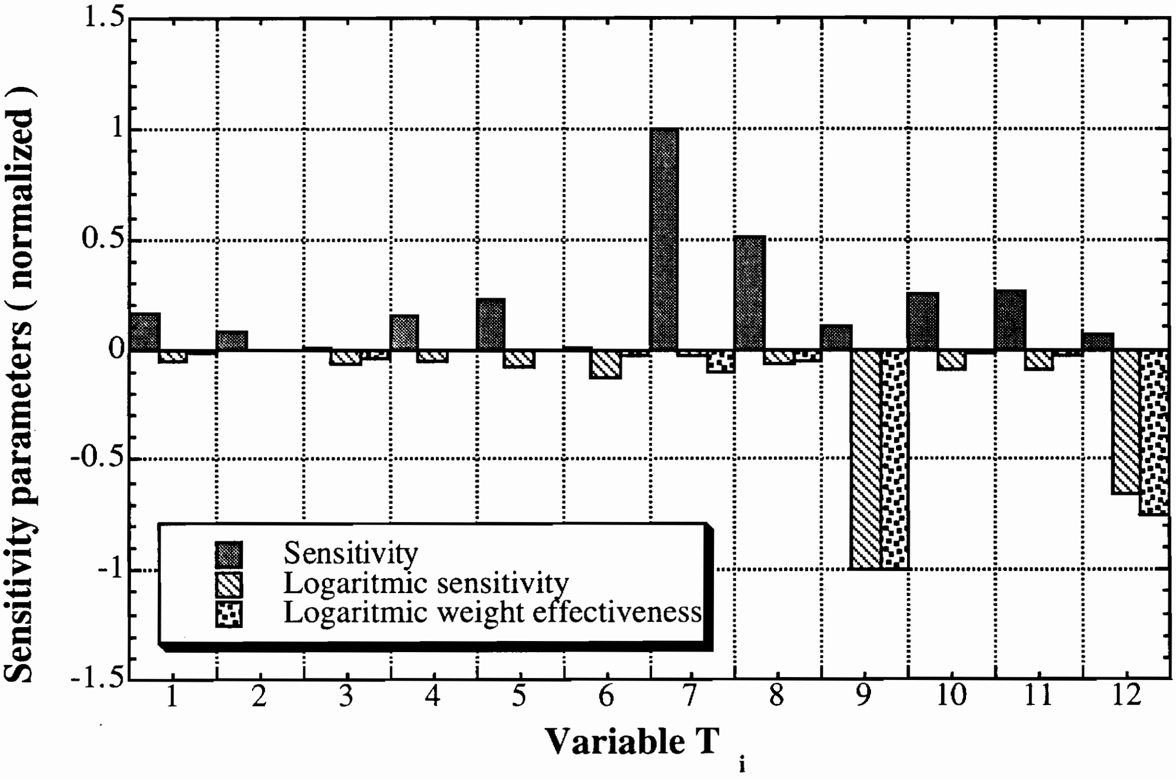

Figure 4.4 - Sensitivities, logarithmic sensitivities and weight effectivenesses for displacement u_4.

The difference between the different parameters is illustrated in Figs. 4.4 and 4.5. Figure 4.4 shows the comparison of the sensitivities with the logarithmic sensitivities and the logarithmic weight effectivenesses for displacement u_4 (top sensor point). Each group of parameters was scaled so that the maximum value is one.

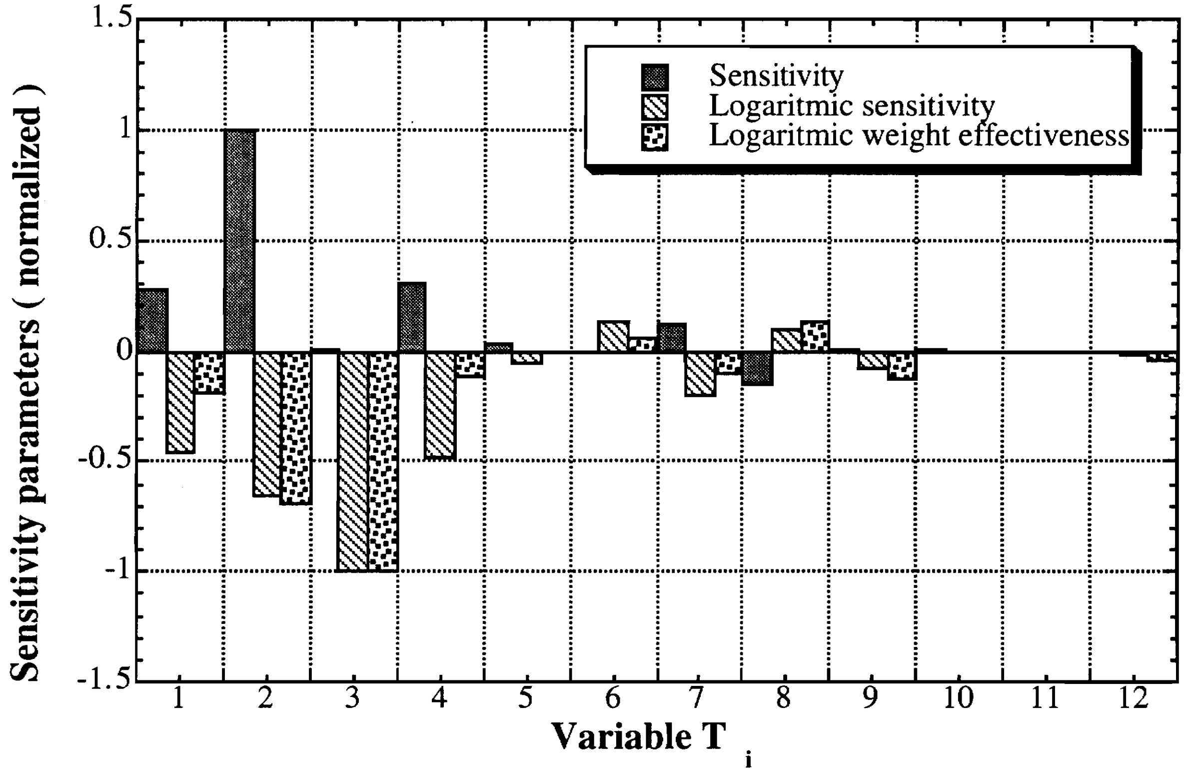

Figure 4.5 - Sensitivities, Logarithmic sensitivities and weight effectivenesses for displacement u_2.

If we just looked at the sensitivities we would conclude that the most important variable T_7, corresponding to one of the plies in the front plate of the interface. The logarithmic sensitivities and the logarithmic weight effectiveness, however, suggest that variables T_9 and T_{12} are the most effective and T_7 is actually not so important. Figure 4.5 shows the comparison of the different parameters for the displacement u_2 (middle snail point). As in Fig. 4.4 different conclusions can be drawn from the displacement dimensional sensitivities and from the logarithmic displacement sensitivities and logarithmic weight effectiveness.

The dimensional displacement sensitivities would suggest to change variable T_2, the unidirectional ply in the back plate of the interface, and do not seem to give much importance to the core of the same plate, variable T_3, which in fact is the driving variable, as suggested by the logarithmic sensitivities.

4.6 Definition of the initial design

In order to succeed in structural optimization, it helps to start from a good initial design, possibly a feasible or near feasible design, i.e. a design that satisfies all the constraints. Although some algorithms are able to start from an infeasible design, with large constraint violations, it is a good rule to start the optimization with a design that lies in, or near the feasible region, or the optimization may fail to find the optimum design.

As can be seen in Table 4.2 the actual design violated the constraints for all five displacements: sensor displacements are about forty times bigger than the allowable values (400 micron vs. 10), while the snails points are from 5 to 60 percent larger then the allowable (10.5 to 15.8 micron vs. 10). To improve the design we followed the indications that came from the sensitivity analysis and we made the following changes:

1 - increased the thickness of the core of the front panel of the interface, and the front and the back panel of the support by 50 percent, from 19 to 28.6 mm;

2 - increased the thickness of the back plate of the interface by 40 percent, from 28.6 to 40 mm;

3 - doubled the thickness of the unidirectional plies of the skins of the back plate of the interface from 0.125 to 0.250 mm.

The results of each of the changes, separately, and of their combination, for the basic set of displacements, are presented in Table 4.8 and compared with the displacements of the original structure. All changes had positive effects on the displacements, although the design is still infeasible. The first three displacements, snail points, are almost all inside the bounds, while the displacements of the sensor points are still far outside those limits.

Table 4.8 - Effect of various design changes on the basic set of displacements.

Units = micron	Original structure	First change only	Second change only	Third change only	All changes (modified structure)
14 along X	-10.5	-10.6	-9.0	-6.4	-5.2
64 along X	-13.9	-13.7	-13.3	-11.3	-10.5
86 along X	-15.8	-15.5	-15.3	-13.1	-12.4
2003 along Z	-391.1	-269.6	-389.1	-389.9	-267.0
2004 along Z	-399.5	-277.9	-397.5	-398.3	-275.3
Weight	45.03	45.72	45.31	45.71	46.69

Table 4.9 shows the complete displacement vector for an extended set of points that includes the basic set of points, shown in Fig. 4.1, and the four connection points between the interface and the support, points 1101 and

1002 on the interface, and points 1201 and 1202 on the support. The extended set of points is shown in Fig. 4.6.

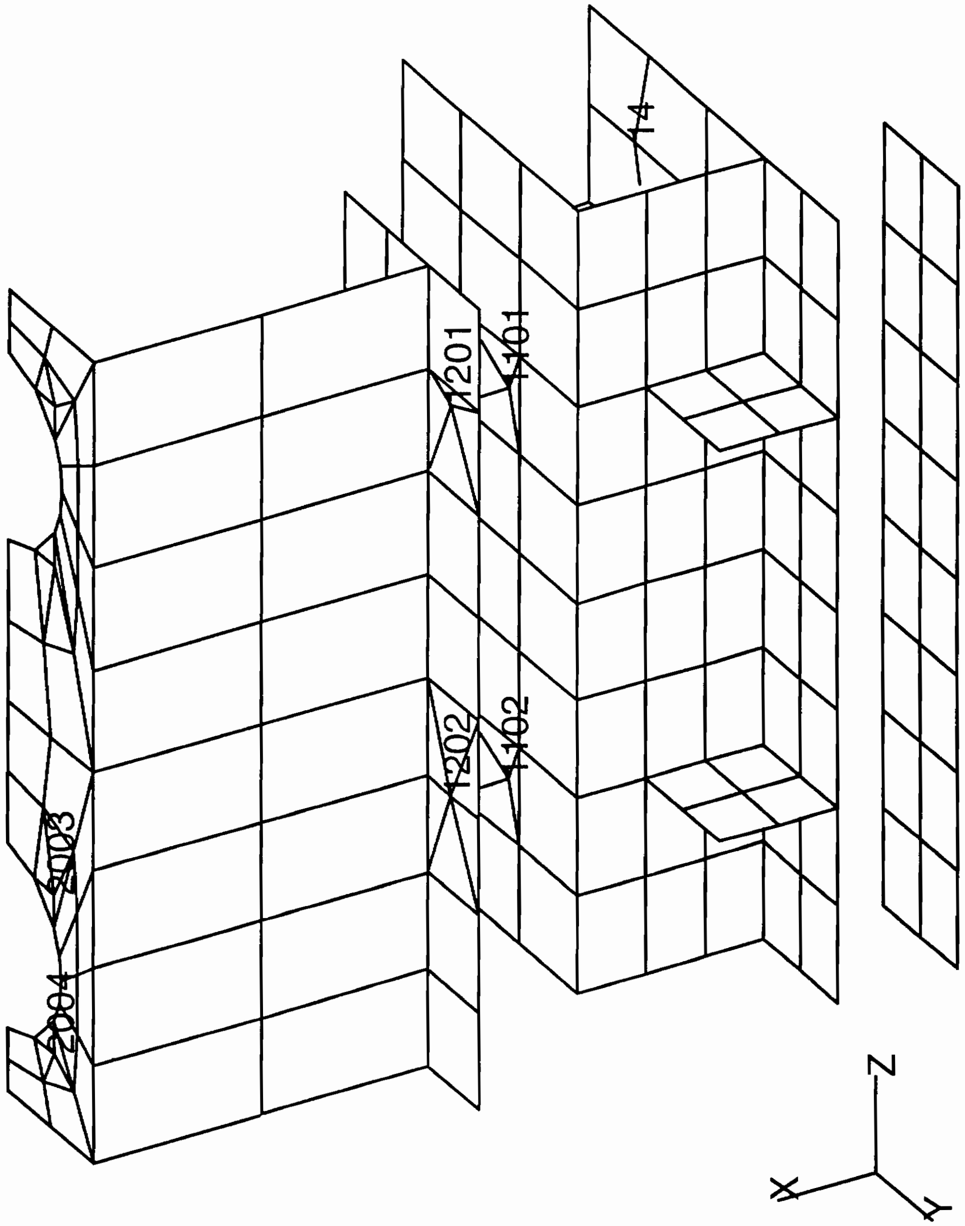

Figure 4.6 - Extended set of points.

Table 4.9 - Displacements of an extended set of points for the modified structure.

Units = micron Node	X	Y	Z
14	-5.2	1.1	0.0
64	-10.5	4.4	0.0
86	-12.4	4.2	0.0
1101	56.2	4.9	-11.2
1102	-62.9	4.8	-34.5
1201	56.2	6.2	-37.7
1202	-62.9	5.5	-54.7
2003	-144.8	2.2	-267.0
2004	-246.2	2.5	-275.3

Examining the displacements of the table, we can make few observations:

1 - the value of the displacements of the sensor points is still far outside the bounds given by the constraints of the optimization, about thirty times bigger than the allowable values;

2 - the value of the Z displacement of points 1101 and 1102 on the front of the interface is considerably smaller than that of the sensor points, indicating that most of the deformation is due to the support;

3 - while the snail points, located on the back panel of the interface, show similar values of the X displacement, the two connecting points 1101 and 1102 on the front panel of the interface present X displacements of opposite sign.

If we look at a plot of the deformed structure, shown in Fig. 4.7, we can clearly see that the displacements at the sensor points are mainly due to a rigid body rotation of the interface about the Y axis. A closer look at the elements surrounding the connecting nodes between the two substructures, reveals large local deformations of the front panel of the interface and of the rear panel of the support. Nodes 1101 and 1201 are pulled out and nodes 1102 and 1202 pushed in, Fig. 4.7, causing the rigid rotation of the support .

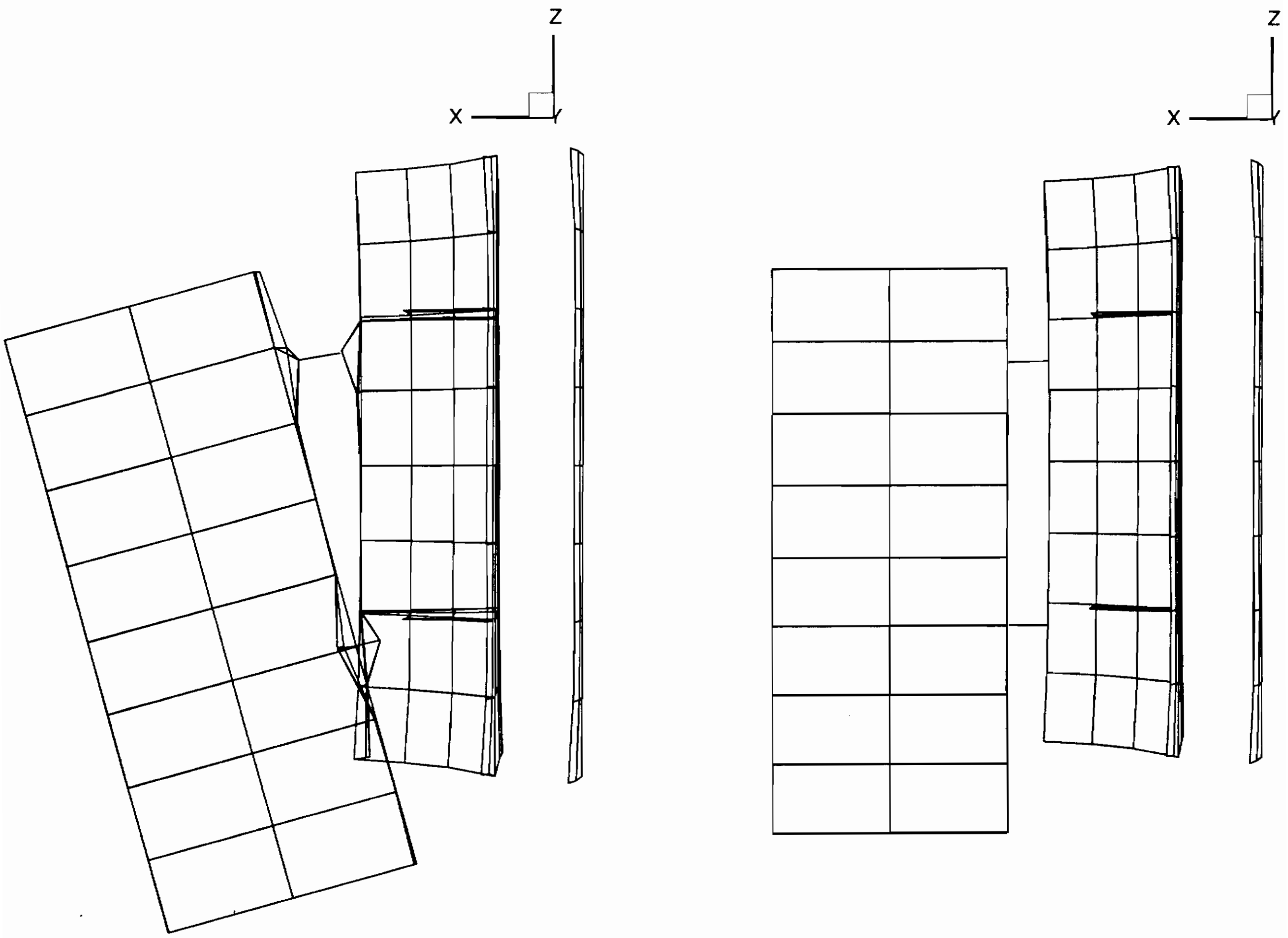

Figure 4.7 - Deformation of the structure: comparison of the deformation when shear effects are considered (left), and when the are neglected (right).

This behavior may be explained by the fact that the model lacks of sufficient refinement in the areas around the connecting nodes, where large transverse point loads are transferred from the support to the interface. In the real carriage the two substructures are connected at four points. At each of these points a metal disc of 30 mm of diameter, Fig 3.1, is bolted on the sandwich panel and bonded on the laminate composite skins. The loads transferred between the interface and the support are thus spread on a surface rather than being concentrated in one point as in the finite element model. The panels are locally reinforced, where the discs are bonded on the skins, with inserts of 30 mm in diameter, so that loads are transferred to both skins. The approximations made in the model can then be summarized as follows:

1 - the loads between the interface and the support are transferred directly only to the nodes immediately adjacent the connection points, instead of being spread on a larger surface;

2 - the contribution to the transverse shear stiffness of the panels given by the inserts is neglected, leading to larger shear deformations. The effects of the transverse shear deformation of the honeycomb core can be seen in Table 4.10, which shows the value of the displacements of the extended set of points of Fig. 4.6 when transverse shear of the honeycomb core is neglected, compared with those, in parenthesis, obtained considering the effects of the core shear deformation.

Displacements at the sensor points, 2003 and 2004, are ten times larger in the Z direction and even more in the X direction, when transverse shear is considered. To correct these problems we tried to model the inserts of the real structure by replacing the honeycomb core with a different material in the property cards of the elements surrounding the points where the real structure is inserted. To reduce localized deformations, and simulate the effect of a distributed load, we used the properties of the woven graphite-epoxy plies as properties of the inserting material.

Table 4.10 - Effects of transverse shear in the honeycomb panels.

Units = micron	X	Y	Z
14	-11.7 (-10.5)	1.2 (1.5)	0.0 (-0.0)
64	-8.6 (-13.9)	5.9 (5.7)	0.0 (-0.0)
86	-10.0 (-15.8)	5.9 (5.6)	0.0 (-0.0)
1101	-2.3 (105.7)	5.3 (5.5)	-3.4 (-12.4)
1102	-1.1 (-119.1)	4.8 (5.3)	-28.7 (-36.4)
1201	2.3 (105.6)	6.3 (6.4)	-9.0 (-57.5)
1202	-1.1 (-119.1)	4.9 (5.8)	-26.7 (-73.6)
2003	7.9 (-252.2)	2.3 (2.2)	-35.5 (-391.1)
2004	-5.2 (-429.8)	2.7 (2.5)	-43.4 (-399.5)

The displacements of the extended set of points of this refined model, that we will call the RM model, are shown in Table 4.11, with, in parenthesis, the corresponding displacements of the original model of the structure, as in Table 4.8. The change in mass of the new model is due to the inserts, replacing the lighter honeycomb core. The effects of the new assumptions on the value of the displacements is substantial. The displacements of the sensor points, dropped by a factor of ten in the Z direction and by about one hundred in the X direction.

Such a drastic change suggests a more refined analysis of the connection between the two substructures, and/or some experimental results that could be compared with those obtained by the present analysis in order to validate the model, or to reveal errors in its formulation. The results obtained with the refined model, however, agreed much better with the good behavior showed by the real carriage during the tests conducted at Speroni. Model RM will then be used in the present analysis.

Table 4.11 - Comparison of the displacements of the refined model RM, and the original model of the structure.

Units = micron	X	Y	Z
14	-5.9 (-10.5)	-1.5 (1.5)	0.0 (-0.0)
64	-11.9 (-13.9)	8.3 (5.7)	0.0 (-0.0)
86	-11.9 (-15.8)	13.2 (5.6)	0.0 (-0.0)
1101	0.3 (105.7)	3.3 (5.5)	-6.5 (-12.4)
1102	-7.4 (-119.1)	2.8 (5.3)	-24.4 (-36.4)
1201	0.3 (105.6)	4.6 (6.4)	-11.6 (-57.5)
1202	-7.4 (-119.1)	3.9 (5.8)	-25.4 (-73.6)
2003	0.9 (-252.2)	1.8 (2.2)	-39.3 (-391.1)
2004	-5.8 (-429.8)	1.7 (2.5)	-49.0 (-399.5)
Weight	55.21 (45.03) N		

For the RM model, the displacements at the snail points, 14, 64, and 86 were only 20 percent higher than the allowable ones, while the displacements at the sensor points were still 4 to 5 times larger than the prescribed limits. The changes in the lay-up of the panels, suggested by the sensitivity analysis that were considered for the original model, Table 4.8, were applied to the refined model RM in order to obtain a feasible design that could be used as initial design in the optimization process.

The results, however, Table 4.12, showed that reasonable increments in the thicknesses of the plies or the cores could not bring the displacements at the sensor points close to the prescribed ten microns. The displacements of this modified design, called MD1, showed a 22 percent decrease in the snail points, but only an 8.3 percent decrease in the sensor points.

Table 4.12 - Effect of various design changes on the basic set of displacements for the RM model.

Units = micron	Refined Model RM	First change only	Second change only	Third change only	All changes, design MD1
14 along X	-5.9	-5.6	-5.8	-4.7	-4.5
64 along X	-11.9	-11.7	-11.2	-9.9	-9.1
86 along X	-11.9	-11.6	-11.7	-9.8	-9.5
2003 along Z	-39.3	-37.1	-38.9	-38.4	-35.6
2004 along Z	-49.0	-46.8	-48.6	-48.2	-45.3
Weight	55.21	57.16	57.46	55.89	60.54

The results displayed in Table 4.11 and a look at the deformed structure suggested that the sensor displacements were caused by three mechanisms:

1 - the rigid rotation of the carriage shown in Fig. 4.7, was still present, although with a smaller magnitude;
2 - a stretching of the support in the Z direction;
3 - a shear deformation of the latter in the X-Z plane.

To limit the effects of the first mechanism, the front panel of the interface and the rear panel of the support were reinforced with woven 0/90 plies and with unidirectional 0° plies. Woven 0/90 plies were also added to the front panel of the support to decrease its deformation in the Z direction, and ±45 woven plies were added to the lateral panel of the support, to increase its shear stiffness.

Table 4.13 - Comparison of the displacements of a modified design MD2 with those of the original design (Table 4.11).

Units = micron, N	X	Y	Z
14	-8.6 (-5.9)	-0.9(-1.5)	0.0 (-0.0)
64	-8.1 (-11.9)	8.2 (8.3)	0.0 (-0.0)
86	-10.8 (-11.9)	12.1 (13.2)	0.0 (-0.0)
1101	-2.6 (0.3)	3.5 (3.3)	-2.5(-6.5)
1102	-5.5 (-7.4)	3.0 (2.8)	-19.8 (-24.4)
1201	-2.6 (0.3)	3.6 (4.6)	-5.8 (-11.6)
1202	-5.5 (-7.4)	3.1 (3.9)	-20.4 (-25.4)
2003	3.25 (0.9)	1.4 (1.8)	-29.5 (-39.3)
2004	-0.8 (-5.8)	1.1 (1.7)	-40.6 (-49.0)
Mass	60.75 (55.21)		

The resulting design, named MD2, gave an average 7.4 percent decrease of the displacements of the snail points, 14, 64, and 86, and an average 20.6 percent decrease for those of the sensor points 2003 and 2004. This reduction required a 10 percent increase in the weight of the carriage. Table 4.13 shows these results compared with those of the original design shown in Table 4.11. While the displacements of the snail points were finally inside the bounds, the sensor point displacements were still three to four times larger than the allowable.

4.7 Optimization

Apparently the task of finding a feasible design for the optimizer was much harder than expected. Doubling or more than doubling the thicknesses of all the skins of the panels produced only a 20.6 reduction of the sensor displacements. At this point we decided on the two following strategies:

1 - Increase the upper bound of the constraint on the sensor points to 30 microns and optimize the structure for minimum weight.
2 - Starting from that optimal design, decrease the limit on displacements to 20 microns, and let the optimizer find a feasible design for us, and eventually restart from this design , and optimize its weight.

The temperature change in both optimizations correspond to 40°C increase in temperature, from 20°C to 60°C. The different optimizations will be labeled basing on the final temperature, and on the value of the limit for the displacement of the sensor points. The first one will then be T60D30, while the second T60D20. Initial and final designs will have the same name of the corresponding optimization with an appended *i* or *f*. For the first optimization, for instance, we will have T60D30i and T60D30f. The original design of Table 4.11 will be referred to as design OD.

The grouping of the panels used for the sensitivity analysis was slightly modified to decrease the number of possible different panels lay-ups in the structure, combining the front and the rear panel of the interface in one group. This reduces the number of variables of the problem, and also reduces the manufacturing cost. The new grouping is shown in Fig. 4.8.

The initial design for the weight minimization was based on the design of Table 4.13. New layers of unidirectional and woven composite with different orientation were added to the laminate skins to let the optimizer consider different possibilities.

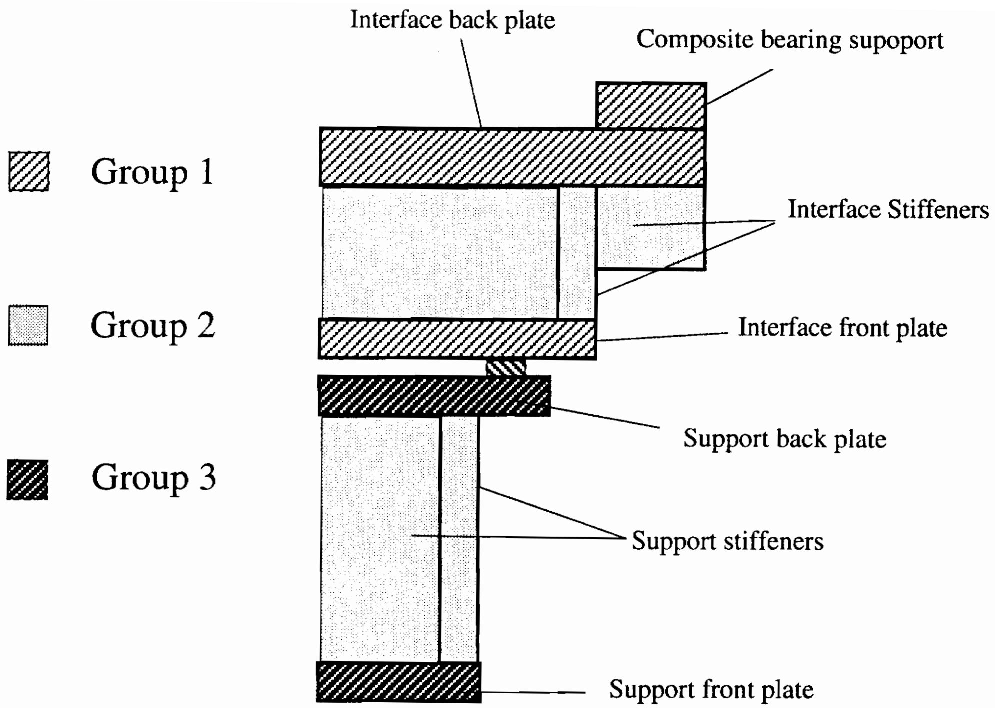

Figure 4.8 - New grouping for the panels of the carriage.

The initial stacking sequences of the initial design T60D30i for the three groups are shown in Fig. 4.9, where for each ply we indicate the corresponding variable number used in the optimization.

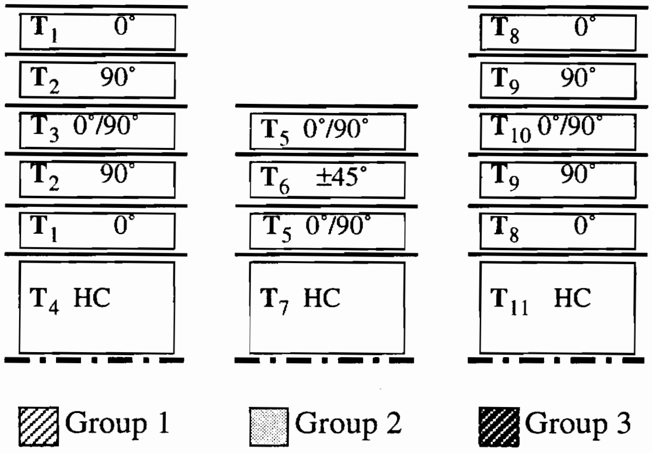

Figure 4.9 - Panel lay-ups for the three groups of panels.

The lower bound for all variables was set to 0.01 mm, which corresponds to the ply being eliminated from the stacking sequence. The upper bound was set to 1 mm for the ply variables and 40 mm for the core variables. The upper bound for the unidirectional plies was somewhat too high, corresponding to eight plies with the same orientation, since this may cause problems due to matrix cracking. This problem, however, was initially not considered to allow a simpler design model.

The optimized design T60D30f allowed a reduction of the weight by about 14 percent with respect to the design T60D30i, starting from 75.5N down to 64.5N, which is, however, a 16.8 percent increase with respect to the weight of the original design OD. The basic set of displacements of the design T60D30f and those of the design OD are compared in Table 4.14.

Table 4.14 - Comparison of the basic set of displacements (microns) of optimized design T60D30f and of original design OD (Table 4.11).

	14 X	64 X	86 X	2003 X	2004 X	Weight
Design OD	-5.9	-11.9	-11.9	-39.3	-49.0	55.21 N
T60D30f	-5.4	-6.1	-8.8	-24.5	-29.9	64.46 N

All the constrained displacements are now inside the bounds of their constraints. However, due to the thermal deformation of the composite plies, other displacements, that were previously disregarded because of their small value, became large enough to deserve some attention. In a future work it may be required to put constraints on displacements other than those so far considered. Table 4.15 compares design T60D30f with design T60D30i in terms of design variables. The optimal design confirmed previous considerations on the mechanisms causing the deformation of the structure.

Table 4.15 - Comparison of the final design T60D30f, with the corresponding initial design T60D30i in terms of design variables (mm).

Group 1			Group 2			Group 3		
	Initial	Final		Initial	Final		Initial	Final
UD 0°	0.50	0.548	Woven 0/90	0.62	0.160	UD 0°	0.50	0.136
UD 90°	0.50	0.109	Woven ±45	1.24	1.406	UD 90°	0.50	0.949
Woven 0/90	0.62	0.339	Woven 0/90	0.62	0.160	Woven 0/90	0.62	0.385
UD 90°	0.50	0.109	Honeycomb	9.50	8.685	UD 90°	0.50	0.949
UD 0°	0.50	0.548				UD 0°	0.50	0.136
Honeycomb	14.3	11.90				Honeycomb	9.50	8.339

The largest design variables increases were in the 0° unidirectional plies of the main panels of the interface, in the ±45° woven plies of the stiffeners and in the 90° unidirectional plies of the main plates of the support. Unlike what suggested by the sensitivity analysis, the thickness of the honeycomb cores decreased, by about a 15 percent.

Next we reduced the value of the allowable displacements for the sensor to 20 microns. Design T60D30f of Table 4.15 was used as the new initial design in the new optimization, named T60D20, as we tried to obtain a feasible design for the new value of the constraints. No feasible design was found this time, because some of the variables reached their upper bound preventing the optimization from reaching the feasible region of the solution space. Results of the optimization T60D20 are presented in Table 4.16. The weight of the carriage increased from the 64.5N of design T60D30f up to 82.2 of the final design T60D20f. This corresponds to a 27.4 percent increase with respect to the initial design, and 48.8 percent increase with respect to the original design OD.

Table 4.16 - Comparison of the basic set of displacements (microns) of optimized design T60D20f and of original design OD (Table 4.11).

	14 X	64 X	86 X	2003 Z	2004 Z	Weight
Design OD	-5.9	-11.9	-11.9	-39.3	-49.0	55.21 N
T60D30f	-1.0	-5.3	-7.3	-17.4	-22.8	82.20 N

In Table 4.17 we show the value of the design variables of the optimized structure compared with those of the initial design. The trend shown in the final design of optimization T60D30 was even more emphasized here, where more than one variable hit the upper bound value of 1 mm. This may become a problem because the number of plies of a practical design derived from both T60D30f and T60D20f would be too high to be considered feasible in terms of manufacturing costs. For each final design an integer number of ply design (INP), was obtained, T60D30-INP and T60D20-INP, by choosing for each stack of plies, in each skin, the number of plies that would give the best approximation to the thickness of the stack in the continuous solution.

Table 4.17 - Comparison of the final design T60D20f, with the corresponding initial design T60D20i in terms of design variables (mm).

Group 1			Group 2			Group 3		
	Initial	Final		Initial	Final		Initial	Final
UD 0°	0.548	0.998	Woven 0/90	0.160	0.525	UD 0°	0.136	0.093
UD 90°	0.109	0.091	Woven ±45	1.406	1.999	UD 90°	0.949	0.998
Woven 0/90	0.339	0.285	Woven 0/90	0.160	0.525	Woven 0/90	0.385	0.999
UD 90°	0.109	0.091	Honeycomb	8.685	11.55	UD 90°	0.949	0.998
UD 0°	0.548	0.998				UD 0°	0.136	0.093
Honeycomb	11.90	17.96				Honeycomb	8.339	7.655

Table 4.18 - Comparison of the Integer Number of Plies designs derived from T60D20f, and T60D20f, with the original design OD in terms of number of plies.

Group 1				Group 2				Group 3			
	OD	D30f-P	D20f-P		OD	D30f-P	D20f-P		OD	D30f-P	D20f-P
0°	1	4	8	0/90	1	1	2	0°	1*	1	1
90°	-	1	1	±45°	2	5	6	90°	-	8	8
0/90	2	1	1	0/90	1	1	2	0/90	2	1	3
90°	-	1	1	HC	9.5	9.50	12.7	90°	-	8	8
0°	1	4	8					0°	1*	1	1
HC		12.7	17.5					HC	9.50	9.50	7.90

* In the design OD we had 0/90 woven plies on the outside and ±45 woven plies in the inside.

D30f and D20f are in place of T60D30-INP and T60D20-INP respectively.

0° and 90° are UD plies while 0/90 and ±45 are woven plies, HC is the honeycomb.

The two INP design are compared with the original design OD in terms of the number of layers in the skins of the different panels. Recall that the thickness of the unidirectional plies is t_{UD}= 0.125 mm, while that of the fabric plies is t_{fabric}= 0.310 mm. In group 1, the 4 plies in the skins of design OD have become 11 in design T60D30-INP and 19 in design T60D20-INP. In group three design T60D20-INP counts 21 plies versus the 4 of design OD.

Table 4.19 - Comparison of the basic set of displacements (microns) of Integer Number of Plies, designs, INP, obtained from design T60D30f and T60D20f and of original design OD (Table 4.11).

	14 X	64 X	86 X	2003 Z	2004 Z	Weight (N)
Design OD	-5.9	-11.9	-11.9	-39.3	-49.0	55.21
T60D30-INP	-2.5 (-58)	-4.5 (-62)	-6.8 (-43)	-23.5 (-40)	-28.9 (-41)	66.92 (+21)
T60D20-INP	-1.1 (-81)	-5.3 (-55)	-6.6 (-45)	-17.7 (-55)	-23.2 (-53)	81.56 (+48)

Table 4.19 shows the results in terms of the basic set of displacements and the weight, for the three designs. The numbers in parenthesis are the percent difference of the displacements and of the weight of the INP designs from those of design OD. Comparing the displacements of the three designs, we see that the changes in the displacements are not comparable to the changes in the thicknesses of the skins of the panels, and are not sufficient to reach the original 4 microns limit set by Speroni, neither the 10 microns limit that we used in the present analysis (see section 4.4). The INP optimum designs, moreover are 21 and 48 percent heavier than design OD.

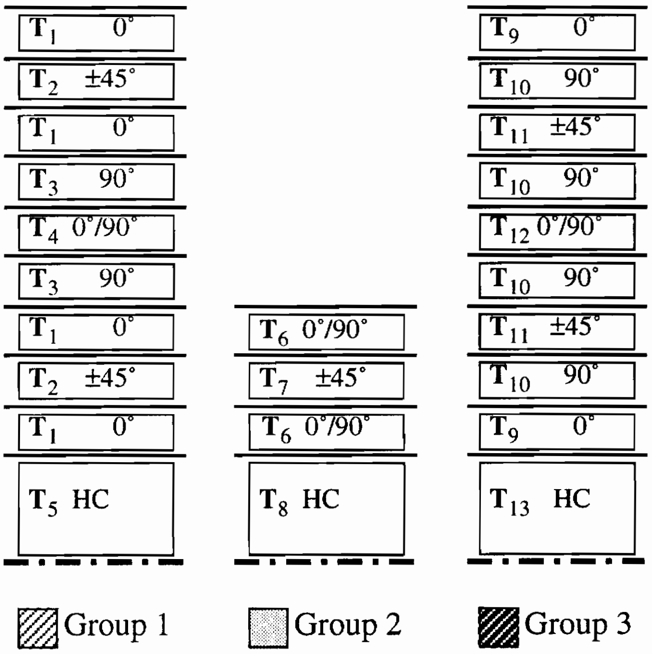

Figure 4.10 - Stacking sequence of initial designs for T45D30 and T45D20.

To improve the design at least from a mechanical point of view, we tried to limit the number of contiguous plies of same orientation, to reduce the risk of matrix cracks. The 0° UD plies in group 1 and the 90° UD plies in group 3 were separated by a woven ±45 ply, and the upper limit for the thickness of the UD plies was reduced to 0.5 mm, corresponding to 4 contiguous plies of the same orientation. Fig. 4.10 shows the new resulting stacking sequences for the three groups. A new optimization, was performed with this new design. The initial design was made up choosing arbitrarily high values for the thicknesses of the plies. We reduced the final temperature to 45°C, which is the maximum temperature for which Speroni guarantees the precision of the machines.

The results of this optimization were surprisingly good. In the first case, T45D30, with the limit on the displacement of the sensor points fixed to 30 microns, the optimizer was able to reduce the weight from 88.2 N of the initial design, to 54.1 N of the optimum design T45D30f, which correspond to a 38.7 percent decrease. With respect to the weight of the original design OD, design T45D30f had a reduction of the mass of about 2 percent.

Table 4.20 - Comparison of the basic set of displacements (microns) of optimized design T45D30f and of original design OD (Table 4.11).

	14 X	64 X	86 X	2003 Z	2004 Z	Weight
Design OD	-5.9	-11.9	-11.9	-39.3	-49.0	55.21 N
T45D30f	-5.1	-7.2	-7.0	-22.1	-26.2	54.06 N

Table 4.20 compares the displacement of T45D30f with the original design OD. The displacements of the snail points are about 35 percent smaller than the original design, and those of the sensor points are almost 50 percent smaller than the original design. Note that it would appear from the table that none of the displacement constraints was active at the optimum design. In fact, the value of the displacements used to check violation of the constraints during the optimization process, is based on linear approximation. The value of the displacements shown in the Tables are

obtained through static analysis of the carriage using the thicknesses of the optimum designs.

Table 4.21 - Comparison of the thicknesses of the final design T45D30f, and the initial design T45D30i (mm).

Group 1			Group 2			Group 3		
	Initial	Final		Initial	Final		Initial	Final
UD 0°	0.50	0.011	Woven 0/90	0.160	0.1063	UD 0°	0.136	0.01
Woven ±45	0.310	0.3031	Woven ±45	1.406	1.078	UD 90°	0.949	0.191
UD 0°	0.50	0.0116	Woven 0/90	0.160	0.1063	Woven ±45	0.385	0.2117
UD 90°	0.50	0.010	Honeycomb	9.50	8.538	UD 90°	0.949	0.191
Woven 0/90	0.310	0.010				Woven 0/90	0.136	0.029
UD 90°	.50	0.010				UD 90°	8.339	0.191
UD 0°	.50	0.011				Woven ±45	0.310	0.2117
Woven ±45	0.310	0.3031				UD 90°	0.500	0.191
UD 0°	0.50	0.011				UD 0°	8.339	0.01
Honeycomb	14.3	9.27				Honeycomb	9.50	9.06

Table 4.21 shows the design variables for T45D30f. Many of the plies decreased their values down to the lower bound of 0.01 mm, and could be removed from the stacking sequence of a practical design. The ±45° woven plies, play a primary role in all panels of the carriage.

Table 4.22 - Comparison of the basic set of displacements (microns) of design T45D20f and the original design OD.

	14 X	64 X	86 X	2003 Z	2004 Z	Weight (N)
Design OD	-5.9	-11.9	-11.9	-39.3	-49.0	55.21
T45D20f	-4.4	-3.5	-6.8	-15.7	-18.7	61.54

A second optimization, T45D20, with a lower value for the displacement of the sensor points, was performed next. Unlike for T60D20, a feasible design was found this time, and unlike T60D20f this design was feasible also from the manufacturing costs point of view. The weight of design T45D20, Table 4.22, was about 30 percent lower than the starting design, and only 11 percent higher than the original design OD. Design T45D20f, however, allowed a remarkable change in the displacements of the carriage. The displacements at the snail points decreased by an average of 50 percent, while those at the sensor points decreased by about 61 percent.

Table 4.23 - Comparison of the final design T45D20f, with the corresponding initial design T45D20i in terms of design variables (mm).

Group 1			Group 2			Group 3		
	Initial	Final		Initial	Final		Initial	Final
UD 0°	0.50	0.049	Woven 0/90	0.160	0.0727	UD 0°	0.136	0.01
Woven ±45	0.310	0.4115	Woven ±45	1.406	1.602	UD 90°	0.949	0.2608
UD 0°	0.50	0.049	Woven 0/90	0.160	0.0727	Woven ±45	0.385	0.4557
UD 90°	0.50	0.010	Honeycomb	9.50	8.705	UD 90°	0.949	0.2608
Woven 0/90	0.310	0.010				Woven 0/90	0.136	0.0100
UD 90°	.50	0.010				UD 90°	8.339	0.2608
UD 0°	.50	0.049				Woven ±45	0.310	0.4557
Woven ±45	0.310	0.4115				UD 90°	0.500	0.2608
UD 0°	0.50	0.049				UD 0°	8.339	0.01
Honeycomb	14.3	11.96				Honeycomb	9.50	9.06

The thicknesses of initial and final designs are compared in Table 4.23. We can see from the table that many variables reached the lower bound for the ply variables, becoming good candidates for being removed from the laminate, while no variable has reached the fixed upper bound. This means smaller number of plies in the laminates, and lower manufacturing costs.

Since a different, lower temperature was used for the last two optimizations, it is reasonable to wonder whether the lower thermal load was the main reason for these good results. To answer this question we optimized T60D20 again with a final temperature of 45°C, named T45D20M. Results of this optimization are compared with T45D20 in Table 4.24.

Table 4.24 - Comparison of the design variables of final designs T45D20f, and T45D20Mf (mm).

Group 1			Group 2			Group 3		
	D20f	D20Mf		D20f	D20Mf		D20f	D20Mf
UD 0°	0.049	-	Woven 0/90	0.0727	0.199	UD 0°	0.01	0.168
Woven ±45	0.4115		Woven ±45	1.602	2.000	UD 90°	0.2608	-
UD 0°	0.049	1.000	Woven 0/90	0.0727	0.199	Woven ±45	0.4557	-
UD 90°	0.010	0.100	Honeycomb	8.705	10.23	UD 90°	0.2608	0.998
Woven 0/90	0.010	0.119				Woven 0/90	0.0100	0.601
UD 90°	0.010	0.100				UD 90°	0.2608	0.998
UD 0°	0.049	1.000				Woven ±45	0.4557	-
Woven ±45	0.4115	-				UD 90°	0.2608	-
UD 0°	0.049	-				UD 0°	0.01	0.168
Honeycomb	11.96	15.70				Honeycomb	9.06	8.149

In group 1 the stack [0°,±45,0°] in T45D20f corresponds to the 0° UD ply of the T45D20Mf, and in group 3 the stack [90°,±45,90°] in T45D20f corresponds to the 90° UD ply of the T45D20Mf. The difference between the two design is noticeable, proving that the temperature is not the main reason for the good performance of design T45D20f. T45D20Mf is about 27 percent heavier than T45D20f, and 41 percent heavier than the original design OD. The continuous solution showed in Table 4.23, must now be converted into an integer number of plies (INP) design, which depends on the available thicknesses of the plies.

4.8 An Integer Number of Plies Optimum Design

A possible INP solution is given in Table 4.25. It is based on design T45D20f, but the plies have been rearranged, so that combination of more than one ply of the same kind could equal a commercial thickness. In the present work we only consider the materials that have been used for the prototype carriage, and so the ply thicknesses are all multiples of 0.125 mm and 0.31 mm.

Table 4.25 - Ply thicknesses (mm) and number of layers for design T45D20-INP.

Group 1		Group 2		Group 3	
Woven ±45	0.31 (1)	Woven ±45	0.93 (3)	Woven ±45	0.31 (1)
UD 0°	0.25 (2)	Woven 0/90	0.31 (1)	UD 90°	0.25 (2)
Woven ±45	0.31 (1)	Woven ±45	0.93 (3)	Woven ±45	0.31 (1)
Honeycomb	12.7	Honeycomb	9.50	UD 90°	0.25 (2)
				Woven ±45	0.31 (1)
				Honeycomb	9.50

The numbers in parenthesis in are the number of layers of each ply. This design provides a 75 percent decrease in the displacements of the sensor points, and a 37 percent decrease in displacement of the snail points, with only a 10 percent increase in the weight. With its relatively low number of plies it is also a good design from the manufacturing cost point of view. Table 4.26 shows the comparison of the INP design with the original OD in terms of displacements.

Table 4.26 - Comparison of the basic set of displacements (microns) of design T45D20-INP and the original design OD.

	14 X	64 X	86 X	2003 Z	2004 Z	Weight (N)
Design OD	-5.9	-11.9	-11.9	-39.3	-49.0	55.21
T45D20-INP	-5.9	-5.1	-7.7	-16.1	-20.5	60.76

As a final study we considered the effects on the displacements of the design of Table 4.24, of the moments given by Speroni for the design of the carriage that were neglected for the present analysis. The complete set of loads is shown in Fig. 2.1. So far only the down ward force **S** was used. The results of the application of the downward moment $\mathbf{M_2}$ is shown in Table 4.27. The difference is quite large, suggesting that the assumption used in the optimization was not well advised.

Table 4.27 - Effects of a new set of loads on the displacements of design T45D20-INP.

	14 X	64 X	86 X	2003 Z	2004 Z	Weight (N)
T45D20-INP	-5.9	-5.1	-7.7	-16.1	-20.5	60.76
New Loads	-3.6	-4.3	-8.8	-27.7	-32.7	60.76

We have to point out, however that the results of the finite element analysis need to be validated with additional tests, and that the improvements allowed by the optimal design would probably hold also with this more complete load set.

5 Concluding Remarks

A composite carriage was designed and built for a Coordinate Measurement Machine (CMM). The composite carriage was found to be about 7 times lighter than its steel counterpart. Successful tests on the machine demonstrated the potential of using composites in CMMs.

Using NASTRAN, finite element models, ranging from single plates to complete carriage, with different mesh sizes were tested to check model accuracy and to find the necessary level of mesh refinement. A fairly coarse mesh was found to give reasonably accurate results. However, results were affected by several modeling details, and among them, transverse shear deformation proved to be very important, and required refinement of modeling of inserts. Uncertainties also remain about fidelity of modeling of joining elements.

A discrepancy was found between the large deformations obtained from the finite element analysis and the perceived excellent performance of the composite carriage during testing. Excessive deformations obtained from the finite element analysis may indicate the need of more accurate testing of the carriage, to validate the finite element model.

Structural optimization of the carriage showed that the displacements of the sensor could be reduced from 50 to 20 microns, with only a 10 percent increase in the weight of the structure. Further reduction, however, may lead to a substantial increase of the weight and the cost of the carriage.

Additional analyses may need to be carried out to validate the adequacy of the optimal solution with respect to multiple loading, different temperature patterns, and dynamic conditions. A validation of the finite element model, however, is a prerequisite to any further analysis.

References

[1] Manzino, P., "Modelli Teorici e Numerici nell'Analisi di Elementi Strutturali a Lastre Multistrato", B.S. Thesis, University of Pavia, Pavia Italy, 1992.

[2] Sprow, E., "High-end CMMs: How much precision do we need ?", Tooling & Production, September 1991, pp. 74-81.

[3] American Cyanamid Co., Test data sheets for Cycom 759 GT2 130, and Cycom 759 1500 Fabric.

[4] EXCEL Co., "TSB 124 Bonded Honeycomb Sandwich Construction", Technical Service Bulletins, 1993.

[5] CIBA-GEIGY, "Redux 410", Instruction Sheet No. RTA. 100a, December 1978.

[6] Tsai, S. W., "Composite Design", 4th Edition, Think Composites, May 1988, pp. B-2 B-3.

[7] Jones, R. M., "Mechanics of Composite Materials", Hemisphere Publishing Corporation, 1975.

[8] Timoshenko, S. P., Woinowsky-Krieger, S., "Theory of Plates and Shells", 2nd Edition, McGraw-Hill International Editions, 1970, pp. 203-205.

[9] Whetstone, J.D., "EISI-EAL Engineering Analysis Language Reference Manual", EISI-EAL System Level 2091, Engineering Information Inc., July 1983.

[10] Kedwart, K.T., "Design Studies", vol. 5, Technomic Publishing Co., Lancaster Pensylvania, 1990.

[11] MSC/NASTRAN Version 67 "Application Manual", The MacNeal Schwendler Co., June 1992, Vol. 1, Sec. 2.12.

[12] MSC/NASTRAN Version 67, "Design Sensitivity and Optimization", The MacNeal Schwendler Co., 1992.

[13] Vanderplaats, G. N., "An Efficient Feasible Direction Algorithm for Design Synthesis", AIAA Journal, Vol. 22, No. 11, November 1984.

[14] MSC/NASTRAN Version 67 "User's Manual", The MacNeal Schwendler Co., August 1991.

Vita

Marco Lombardi was seen for the first time in Cremona, Italy, on October 6 1966. Desperation of his kindergarten teacher as well as his elementary teacher, he progressively improved his relations with the rules of the common good, and some of his high school professors even considered him as a very serious person. He obtained his first degree (5 years program) in Structural Engineering at the University of Pavia, Pavia, Italy in 1991. At the end of the same year he enrolled in the Doctorate Program at the Polytechnic of Milano, Italy, and one year later, in the spring of 1993 he enrolled in the Master Program in Aerospace Engineering at Virginia Polytechnic Institute and State University, Blacksburg, Virginia. He completed his master studies in the summer of 1994. He is going to complete his doctorate degree in the spring of 1995.

Marco Lombardi

" **What's up Doc ?** "

Bugs Bunny